J. Fluid Mech. (1994), *vol.* 275, *pp.* 83–119
Copyright © 1994 Cambridge University Press

On the properties of similarity subgrid-scale models as deduced from measurements in a turbulent jet

By SHEWEN LIU, CHARLES MENEVEAU AND JOSEPH KATZ

Department of Mechanical Engineering, The Johns Hopkins University, Baltimore, MD 21218, USA

(Received 19 November 1993 and in revised form 7 March 1994)

The properties of turbulence subgrid-scale stresses are studied using experimental data in the far field of a round jet, at a Reynolds number of $R_\lambda \approx 310$. Measurements are performed using two-dimensional particle displacement velocimetry. Three elements of the subgrid-scale stress tensor are calculated using planar filtering of the data. Using *a priori* testing, eddy-viscosity closures are shown to display very little correlation with the real stresses, in accord with earlier findings based on direct numerical simulations at lower Reynolds numbers. Detailed analysis of subgrid energy fluxes and of the velocity field decomposed into logarithmic bands leads to a new similarity subgrid-scale model. It is based on the 'resolved stress' tensor L_{ij}, which is obtained by filtering products of resolved velocities at a scale equal to twice the grid scale. The correlation coefficient of this model with the real stress is shown to be substantially higher than that of the eddy-viscosity closures. It is shown that mixed models display similar levels of correlation. During the *a priori* test, care is taken to only employ resolved data in a fashion that is consistent with the information that would be available during large-eddy simulation. The influence of the filter shape on the correlation is documented in detail, and the model is compared to the original similarity model of Bardina *et al.* (1980). A relationship between L_{ij} and a nonlinear subgrid-scale model is established. In order to control the amount of kinetic energy backscatter, which could potentially lead to numerical instability, an *ad hoc* weighting function that depends on the alignment between L_{ij} and the strain-rate tensor, is introduced. A 'dynamic' version of the model is shown, based on the data, to allow a self-consistent determination of the coefficient. In addition, all tensor elements of the model are shown to display the correct scaling with normal distance near a solid boundary.

1. Introduction

An important problem for the large-eddy simulation (LES) of turbulent flows is the parametrization of the subgrid scales as a function of the resolved flow variables. This problem has been receiving considerable attention in recent years owing to the increasing possibilities of engineering applications of LES (see e.g. Akselvoll & Moin 1993 and other contributions appearing in that volume), and owing to recent developments in modelling (Germano *et al.* 1991; Lilly 1992; Piomelli 1993 among others).

The basic concepts and initial experiments with LES are described in Smagorinsky (1963), Lilly (1967) and Deardorff (1970). Further developments and applications can be found in Schumann (1975), Ferziger (1977), Clark, Ferziger & Reynolds (1979), Bardina, Ferziger & Reynolds (1980), Piomelli, Moin & Ferziger (1988), Yoshizawa

(1989), Schmidt & Schumann (1989), Métais & Lesieur (1992), and Horiuti (1993). For analytical treatments of subgrid-scale (SGS) modelling, see e.g. Leonard (1974), Kraichnan (1976), Leslie & Quarini (1979), Chollet & Lesieur (1981), Chasnov (1981). Rogallo & Moin (1984) and Reynolds (1990) give reviews of the field.

Let us consider an incompressible turbulent flow obeying the Navier–Stokes equations. It follows that $\tilde{u}_i(\boldsymbol{x}, t)$ the convolution (denoted by a tilde) of the velocity field with some spatial filter of characteristic width Δ (or some anisotropic filter with widths Δ_i in each direction, $i = 1, 2, 3$), obeys the filtered Navier–Stokes equations

$$\frac{\partial \tilde{u}_i}{\partial x_i} = 0, \tag{1}$$

$$\frac{\partial \tilde{u}_i}{\partial t} + \tilde{u}_j \frac{\partial \tilde{u}_i}{\partial x_j} = -\frac{\partial}{\partial x_j}\left[\frac{\tilde{p}}{\rho}\delta_{ij} + \tau_{ij}\right] + \nu \nabla^2 \tilde{u}_i. \tag{2}$$

The SGS stress tensor τ_{ij} is defined as

$$\tau_{ij} \equiv \widetilde{u_i u_j} - \tilde{u}_i \tilde{u}_j, \tag{3}$$

where, on purpose, we have not subtracted the trace. In order to successfully solve (2) on a computational mesh with a grid size of the order of Δ, one needs to parametrize $\tau_{ij}(\boldsymbol{x}, t)$ in terms of the resolved velocity field $\tilde{u}_i(\boldsymbol{x}, t)$. We shall denote such a model by the tensor $\mathscr{T}_{ij}[\tilde{\boldsymbol{u}}]$.

One method of investigating the correctness of an SGS model is to perform the simulation for a particular flow and then compare the results with experimental data (commonly referred to as *a posteriori* model testing, as coined in Piomelli *et al.* 1988). Another approach consists of using fully resolved velocity fields to compare the local instantaneous subgrid stress with the prediction of a subgrid-scale model. This approach, frequently called *a priori* testing (Piomelli *et al.* 1988), was pioneered by Clarke *et al.* (1979) and McMillan & Ferziger (1979) through the analysis of fields obtained from direct numerical simulations (DNS). With this approach, it has been repeatedly observed that the eddy-viscosity closures in general, and the Smagorinsky model

$$\mathscr{T}_{ij}^{(S)} = -2(c_s \Delta)^2 |\tilde{S}| \tilde{S}_{ij} \tag{4}$$

in particular, display very little correlation with the real stress τ_{ij}. On a local and instantaneous basis, these two tensors are almost never the same. Nevertheless, this need not be a problem *per se* for the LES prediction of the correct flow statistics, and the relative success of LES in this regard points to considerable robustness of the LES equations. Meneveau (1994) derived a set of necessary conditions on the modelled stress that make correct LES statistics possible, and showed, in grid turbulence, that eddy-viscosity closures do follow these conditions surprisingly well.

On the other hand, a model which could be shown to also display a high correlation between τ_{ij} and $\mathscr{T}_{ij}$ during *a priori* tests would be more desirable. Among other things, the predictability of individual flow realizations could be enhanced with instantaneously more realistic models. Such a feature is of relevance to, for example, active control of turbulent flow. Along these lines, it can be argued that the most well-known model to have resulted from *a priori* analysis of DNS data is the similarity model of Bardina *et al.* (1980). Using the observation that the filtered value of the fluctuating velocity $u_i' \equiv u_i - \tilde{u}_i$ can be written as

$$\tilde{u}_i' = \tilde{u}_i - \tilde{\tilde{u}}_i \tag{5}$$

it was postulated that $\mathscr{R}_{ij}$, the SGS Reynolds stress ($= \widetilde{u_i' u_j'}$), could be approximated as

$$\mathscr{R}_{ij} = (\tilde{u}_i - \tilde{\tilde{u}}_i)(\tilde{u}_j - \tilde{\tilde{u}}_j). \tag{6}$$

After a similar argument is made for the cross-stresses, and after addition of the Leonard stress, the Bardina similarity model reads

$$\mathscr{T}_{ij}^{(B)} = \widetilde{\tilde{u}_i \tilde{u}_j} - \tilde{\tilde{u}}_i \tilde{\tilde{u}}_j. \tag{7}$$

This model (and several of its variants) has been repeatedly shown to exhibit considerable correlation with the real stress during *a priori* tests (Bardina *et al.* 1980; Piomelli *et al.* 1988; Horiuti 1989, etc.). However, when implemented in LES calculations, the addition of eddy-viscosity terms was always found to be necessary in order for sufficient energy dissipation to take place.

A fundamental drawback of *a priori* analysis based on DNS data is the restriction to low Reynolds numbers. Thus both of the above conclusions (low correlation coefficients for eddy-viscosity closures and high correlations for the Bardina model) are based on data that are representative of high-Reynolds-number flows only under relatively strong assumptions. To overcome this difficulty, one can consider experimental data, where substantially higher Reynolds numbers and/or more complex flows can be considered. Experimental data are not without their problems, however, as only partial information about the flow is accessible, depending on the measurement technique.

The present work is an experimental *a priori* study of SGS modelling. The choice of what type of flow to study is dictated by the need to consider as high a Reynolds number as possible. The far field of a jet provides reasonably high Reynolds numbers (we will find $R_\lambda \sim 310$) within a moderately sized facility. This is unlike grid-generated turbulence, where relatively low fluctuating velocities typically lead to lower microscale Reynolds numbers. The next important step in the proposed methodology is to obtain as complete information about the flow field as possible. The technique of particle displacement velocimetry (PDV) allows us, at present, to measure the projection of the velocity vectors onto two-dimensional sections of the flow. The experimental set-up and the instrumentation are described in §2. In §3, the data's kinetic energy spectrum is documented, and we verify that we are adequately resolving the inertial-range scales of interest. Section 4 describes a study of the Smagorinsky model and of the rate of kinetic energy dissipation accomplished by the SGS stress. We then study the energy flux to different ranges of small scales, which motivates us to perform a decomposition of the velocity field into distinct bands.

In §§5 and 6 a systematic study of flow features at different lengthscales is used to propose a new similarity SGS model. The correlation coefficient between this similarity model and the real stress is measured, and the influence of different filters is documented. Particular emphasis is placed on performing the analysis using only data that are consistent with that available during an LES (an approach which we shall call a *consistent a priori* test). The tests are made more complete by comparatively applying them to Gaussian fields with random phases, displaying a white-noise or a $-\frac{5}{3}$ energy spectrum.

After having established these basic results from the experimental data, in the next sections (7–9) we discuss some of the properties of the model and propose some possible modifications. There, the experimental data are used to support and illustrate the discussion rather than to arrive at the results. First we establish connections to nonlinear models based on the resolved velocity-gradient tensor (§7). Second, in §8, we introduce a means of controlling the amount of backscatter, and amend the similarity model derived before. This *ad hoc* modification yields a dissipative similarity model.

Application of the dynamic procedure of Germano *et al.* (1991) and the near-wall scaling of the SGS stress are discussed in §9. A summary of the results and the basic conclusions are given in §10.

2. Experimental set-up

2.1. *Facility*

As noted before, our objective is to generate turbulent flow with R_λ as high as possible, but within a moderately sized facility. Of the possibilities considered, the far field of a turbulent jet seems to be the simplest and most flexible option. A schematic description of the test facility is presented in figure 1(*a*). It consists of a water jet of diameter $D =$ 6.3 mm, which is injected into a 71×71 cm wide and 183 cm long chamber that has windows on all sides. Turning vanes, honeycomb and screens, as well as a smooth cosine shaped nozzle are used for control of turbulence and uniformity of the jet. A large honeycomb at the bottom of the chamber is used for reducing the effect of the exit pipe. The flow is driven by a $\frac{1}{2}$ hp centrifugal pump, that is attached to the rest of the facility with 1 m long flexible hoses to reduce the impact of vibrations. The available power of the pump enables injection speeds of up to 18 m s^{-1} at the nozzle. The experiments are performed at 15 m s^{-1} ($Re_D = 9.5 \times 10^4$). All the measurements are performed in the centreplane of the facility. The square, 7×7 cm, sample area is centred 193 diameters downstream of the nozzle. Its size ($L = 7$ cm) is chosen to approximately match the integral scale of turbulence at this downstream location. Employing the usual estimates for a round jet (Tennekes & Lumley 1972), the flow integral scale at $x_1/D = 193$ is $l \approx 7$ cm.

2.2. *Instrumentation*

Velocity measurements are performed using particle displacement velocimetry. A schematic description of the optical set-up is presented in figure 1(*b*). The light source is a 30 W copper vapour laser (out of which about 20 W are green – 511.5 nm, and 10 W are yellow – 578 nm). A dichroic filter is used to filter out the yellow beam, which enables better focusing into a narrow sheet. The beam diameter is reduced to about 1 mm and then expanded into a thin sheet with a cylindrical lens. To obtain acceptable levels of resolution, the images are recorded by a Hasseblad film camera, which has an image size of 56×56 mm on the film. It is equipped with a 120 mm lens and extension tubes, which enables the recording of data at a magnification factor of 0.65. Thus, the image covers an area of 8.6×8.6 cm, out of which 7×7 cm are used during the analysis. Photographs are recorded on TMAX ASA 3200 film. Coordination between the camera and the laser is achieved using a control system (Ganapathy & Katz 1993) hosted by a personal computer. Typically, triple-exposure images are recorded. The duration of each laser pulse is 40 ns, and the delay between pulses is 0.675 ms. Spherical fluorescent particles, 20 μm in diameter, are used as velocity tracers (Dong, Chu & Katz 1992). These particles are manufactured in our laboratory and have a specific gravity ranging between 0.95 and 1.1. At this size, and owing to the velocities involved, the relative velocity between the particles and the fluid is insignificant. The entire facility is flooded with these particles.

The negatives are scanned using a Nikon LS 3500, 35 mm slide scanner. Owing to its large size, each negative must be scanned in six separate portions. These portions are then matched, by comparing the location of several particles chosen as reference. The error introduced through this procedure is negligible. Overall, each negative is converted to a 5000×5000 pixels array, which is then filtered and enhanced. The

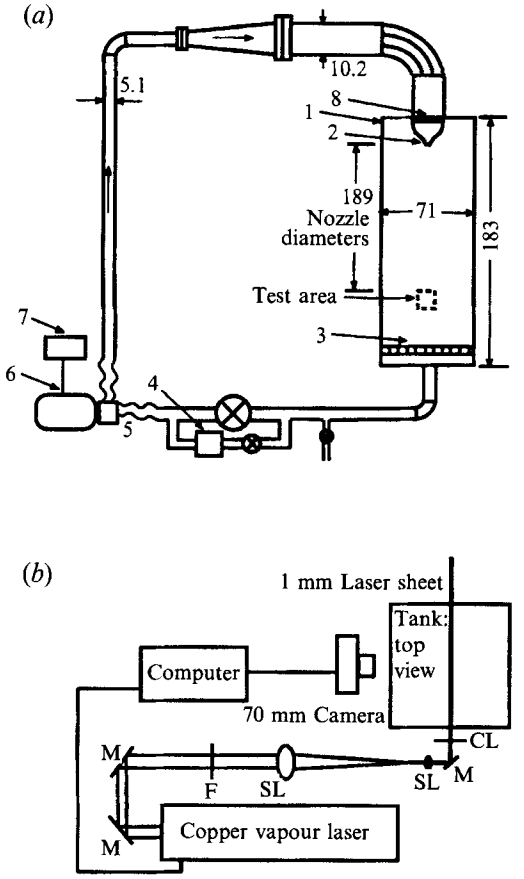

FIGURE 1. Schematic of the experimental set-up. The facility is shown in (*a*): 1, tank; 2, nozzle (D = 0.635 cm); 3, honeycomb; 4, filter; 5, flexible hose; 6, pump; 7, speed control; 8, honeycomb & screen. All dimensions are in cm. The optical instrumentation is shown in (*b*): M, mirror; SL, spherical lens; CL, cylindrical lens; F, filter.

autocorrelation method, described in detail by Dong *et al.* (1992) is used for computing the velocity. Each vector is determined from a 64 × 64 pixels array, which corresponds to a 1.1 × 1.1 mm window in the actual flow field. The velocity is evaluated every 32 pixels (the smallest grid spacing, denoted by δ), which means that 50 % of neighbouring windows overlap. Sub-pixel accuracy (about 0.2 pixels) is achieved by interpolating between the discretely computed values of the auto-correlation function. Problems occur occasionally (in less than 0.3 % of the windows) when the particle density is low, or when a particularly bright particle is present. To correct for these cases, the analysis procedure includes detailed comparisons between neighbouring vectors. Whenever their difference exceeds a pre-determined threshold, the correlation peaks are recalculated using either enlarged or slightly shifted windows. Only images where every vector can be determined, corrected or corroborated in this fashion, are used in the present study. No interpolation is employed to make up for incomplete data.

Based on calibration experiments performed by Dong *et al.* (1992), the error in our method is about 1 % of the velocity, provided each interrogation window contains at least 8 particle pairs. This requirement dictates the required particle density in the test facility, of at least 7 mm^{-3}. The corresponding volume fraction, $< 0.003\,\%$, is still below any level that affects the flow structure and turbulence characteristics.

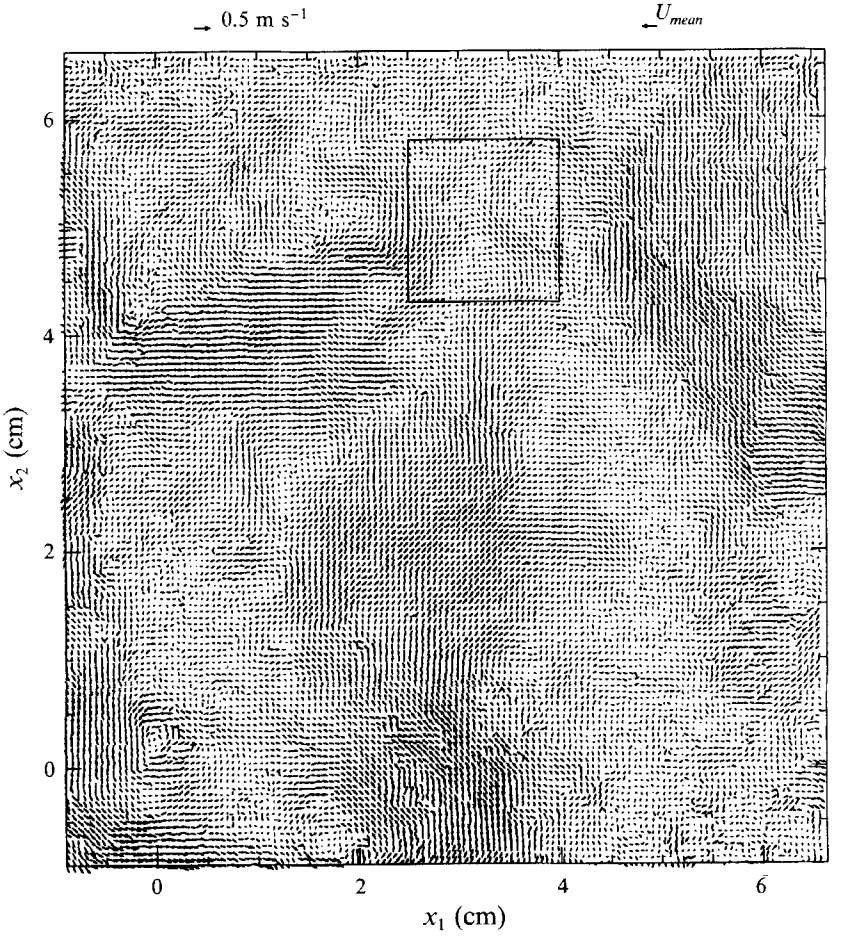

FIGURE 2. Instantaneous velocity vectors projected onto an axial plane in the far field of a turbulent round jet. There are 128 × 128 vectors. The mean velocity of the image (shown on the top right) is from right to left, and has been subtracted from each vector. The velocity scale is indicated on the top left.

Computations are performed on an IBM RS/6000 workstation. On this computer it typically takes about 30 minutes to calculate 2000 vectors from an 8 bit image, including data evaluation, comparison to neighbouring vectors etc. Thus, a single vector map containing 128 × 128 vectors takes about 4 hours CPU time to analyse. In the present paper we have opted to present results obtained from six images.

3. Flow characterization

In this section, the basic features of the flow are described. Figure 2 is a typical velocity map after the mean velocity has been subtracted. The mean velocity, computed over the entire image, is in the $-x_1$ direction. Turbulent motion is visible over a wide range of lengthscales. This feature is illustrated by considering the portion of the flow enclosed in the square, which is shown in figure 3 in an enlarged format. Although the jet continues to develop from the right to the left portion of the imaged region, in the present study we neglect the spatial inhomogeneity of the flow statistics within the

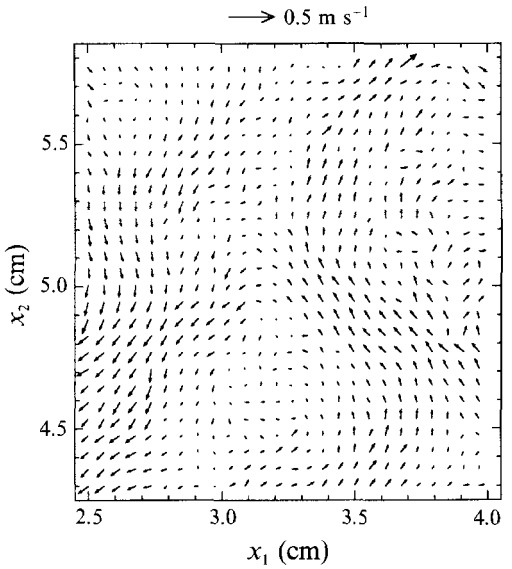

FIGURE 3. Enlarged portion of figure 2, showing details of the turbulent flow field.

image. This approximation is warranted since the changes in mean quantities are small compared to the turbulence quantities (e.g. according to usual estimates the mean and root-mean-square velocities at the centreline will change only by about 5%). Therefore we accumulate statistics over the entire image (excepting some regions close to the edges, as explained later). Furthermore, in order to improve statistical convergence, six images will be employed for all averages presented in this paper, unless stated otherwise.

The mean streamwise velocity in the imaged region is $U_{mean} = -0.5$ m s^{-1}, while the velocity root-mean-square (r.m.s.) values in the streamwise and transverse directions are $u_1' = u_2' = 0.09$ m s^{-1}. The dissipation rate per unit mass, estimated as $\epsilon \approx u_1'^3/l$, is $\epsilon \approx 0.011$ m^2 s^{-3}. An estimate for the average value of the Kolmogorov scale in the region of interest is $\eta = (\nu^3/\epsilon)^{1/4} \approx 0.1$ mm. The Taylor microscale is estimated by $\lambda \approx u_1'(15\nu/\epsilon)^{1/2} \approx 3.4$ mm. Therefore, the microscale Reynolds number is $R_\lambda \approx 310$, which is considerably higher than that of DNS data sets that have been previously employed to study SGS models.

The spectral properties of the flow are now described. We consider the radial two-dimensional spectrum, defined by a sum over an annulus with radius k in wavenumber space:

$$E_{ii}(k) = \sum_{k_1^2+k_2^2=k^2} u_i(k_1,k_2)\, u_i^*(k_1,k_2) \quad \text{(no summation in } i\text{)}, \tag{8}$$

where

$$u_i(k_1,k_2) = \sum_{m=1}^{128}\sum_{n=1}^{128} u_i(x_{1m},x_{2n},[x_3]_0)\, W(x_{1m},x_{2n})\, \mathrm{e}^{-\mathrm{i}(x_{1m}k_1+x_{2n}k_2)} \tag{9}$$

is the two-dimensional Fourier transform of the velocity field in the plane $x_3 = [x_3]_0$. Furthermore,

$$W(x_{1m},x_{2n}) = \left(1-\frac{m-\frac{1}{2}(M-1)}{\frac{1}{2}(M+1)}\right)^2\left(1-\frac{n-\frac{1}{2}(N-1)}{\frac{1}{2}(N+1)}\right)^2 \quad (M=N=128)$$

is a (Welch) windowing function which is needed because the data are not periodic. The

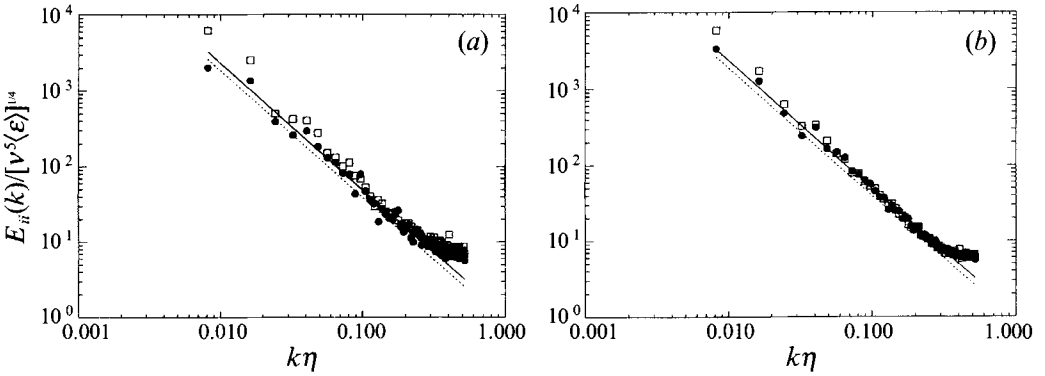

FIGURE 4. (*a*) Radial two-dimensional energy spectrum in Kolmogorov units, of the vector field shown in figure 2. Circles and squares are for the u_1 and u_2 components, respectively. Lines show the Kolmogorov spectrum (without a dissipation range), for $C_k = 1.6$ (dotted line) and $C_k = 2$ (solid line). (*b*) Same as (*a*), but averaged over all six images.

spectrum that results from the velocity field of figure 2 is shown in figure 4(*a*), in Komolgorov units. For comparison, the solid and dotted lines show the inertial-range behaviour of the Kolmogorov spectrum, $E_{ii}(k) = \beta C_k k^{-5/3}$, for two different values of the Kolmogorov constant ($C_k = 2.0$ and $C_k = 1.6$). The coefficient $\beta = 0.535$ accounts for the fact that we are dealing with a two- and not a three-dimensional radial spectrum (see Appendix A). Several observations can readily be made. (i) A significant portion of the spectrum (over a decade) is consistent with a $-\frac{5}{3}$ power-law decay. (ii) The implied value of the Kolmogorov constant ($C_k = 2.0$) is within the range of accepted values, although on the high side. However, since this constant depends strongly on the estimate of ϵ, which itself is very approximate, not much significance can be ascribed to the implied value of C_k. (iii) Finally, the dissipation range is not resolved in these data, which is not surprising if we recall that our spatial resolution (given by the width of the sampling windows) is, by design, approximately 10η. In order to eliminate some of the scatter in the spectrum, it can recomputed by averaging over all six images. The result is shown in figure 4(*b*), confirming that the above conclusions are valid for the ensemble as well. We now comment on the noise which is visible at high wavenumbers. An estimate of the expected level of the noise floor can be obtained by noticing that an experimental uncertainty of 1 % of the mean velocity translates in this case into an uncertainty of about 5 % of the r.m.s. velocity. Thus one can expect a noise floor at $0.05^{-2} \approx 2.5$ decades below the peak of the energy spectrum, consistent with the results in figure 4. This noise floor is not a serious limitation for the purposes of the present study, since we are interested in filtering the data at lengthscales pertaining to the inertial range and do not have any direct interest in the dissipative range.

4. Basic statistics of SGS stresses

In this section we give some basic definitions related to the filtering. Also, the method of calculating the subgrid stress is described, and we document some of its fundamental properties.

4.1. *Definitions*

The filtered velocity field is formally defined as

$$\tilde{u}(x_1, x_2) = \int_{-\infty}^{\infty}\int_{-\infty}^{\infty} u_i(x_1', x_2')\, F_\Delta(x_1 - x_1', x_2 - x_2')\, \mathrm{d}x_1'\, \mathrm{d}x_2' \quad (i = 1, 2), \tag{10}$$

where $F_\Delta(x_1, x_2)$ is a spatial low-pass filter with characteristic width Δ. We notice that the filtering is a two-dimensional one, instead of the three-dimensional filtering that is possible when analysing DNS data. We shall comment on the limitations and interpretation of this two-dimensional filtering in §4.2. The discrete filtering is performed using the fast Fourier transform on the measurement grid. The filters that will be employed are

top hat:
$$F_\Delta(x_1, x_2) = \begin{cases} K_1 & \text{if } |x_1| < \tfrac{1}{2}\Delta \text{ and } |x_2| < \tfrac{1}{2}\Delta \\ 0 & \text{otherwise;} \end{cases} \tag{11}$$

Gaussian:
$$F_\Delta(x_1, x_2) = K_2 \exp[-6(x_1^2 + x_2^2)/\Delta^2]; \tag{12}$$

cut-off:
$$F_\Delta(x_1, x_2) = K_3 \frac{\sin(\pi x_1/\Delta)}{\pi x_1/\Delta} \frac{\sin(\pi x_2/\Delta)}{\pi x_2/\Delta}. \tag{13}$$

The coefficient K_l is a normalization factor which ensures that the integral of the filter equals unity (in the discrete sense). With regard to end effects that need to be taken into account for the filtering, we adopt the following procedures. For the top-hat filter, we only analyse the data in an interior region of size $L-\Delta$ (recalling that $L = 7$ cm), so that no errors are generated at the boundaries. The other two filters (Gaussian and cut-off) have long tails. We adopt the following dual strategy. (i) The data are extended by assuming them to be symmetric with respect to the edges of the domain ($u_i(-x_1, x_2) = u_i(x_1, x_2)$ and $u_i(L+x_1, x_2) = u_i(L-x_1, x_2)$, and similarly in the x_2 direction). In this manner, discontinuity of the data is avoided. (ii) Furthermore, statistics are accumulated only over an interior subset of size $L-\Delta$, for which the edge effects are small. For the Gaussian filter, the truncated portion of the filter corresponds to a tail starting at $x/\Delta = 0.5$. This tail contains only 4% of the total area under the filter function. For the cut-off filter (which we shall not use very frequently) we recognize that the errors involved are more significant because of its slow $1/x$ decay.

A typical filtered velocity-vector field is shown in figure 5, using the top-hat filter with a filter size of $\Delta = 8\delta \sim 48\eta$. As can be seen, the small-scale motion has been smoothed out.

Similarly, the SGS stress elements τ_{ij} are computed according to

$$\tau_{ij}(x_1, x_2) = \int_{-\infty}^{\infty} \int_{-\infty}^{\infty} u_i(x_1', x_2')\, u_j(x_1', x_2')\, F_\Delta(x_1 - x_1', x_2 - x_2')\, \mathrm{d}x_1'\, \mathrm{d}x_2' - \tilde{u}_i(x_1, x_2)\, \tilde{u}_j(x_1, x_2) \quad (i,j = 1,2). \tag{14}$$

The resolved velocity-gradient tensor $\tilde{A}_{ij}$ is defined as

$$\tilde{A}_{ij} = \partial \tilde{u}_i / \partial x_j, \tag{15}$$

while the resolved rate-of-strain elements and measured vorticity component are

$$\tilde{S}_{ij} = \tfrac{1}{2}(\tilde{A}_{ij} + \tilde{A}_{ji}), \quad \tilde{\omega}_3 = (\tilde{A}_{12} - \tilde{A}_{21}). \tag{16}$$

We will frequently use the fields $\tilde{u}_i$ and τ_{ij} 'sampled' on a coarse mesh with a spacing of Δ. The nodes of this mesh are located at $([x_1]_0 + j_1\Delta, [x_2]_0 + j_2\Delta)$, where ($j_1 = 0, 1, 2, \ldots; j_2 = 0, 1, 2, \ldots$), and where the point $([x_1]_0, [x_2]_0)$ is a reference point. Occasionally we shall consider averages over all possible reference points.

4.2. *Interpretation of filtering*

In the context of the *a priori* analysis to follow in this paper, the measured values of $\tilde{u}_i$ and τ_{ij} will be employed quite frequently. It is therefore pertinent to give, at this point in the development, a precise interpretation of these variables.

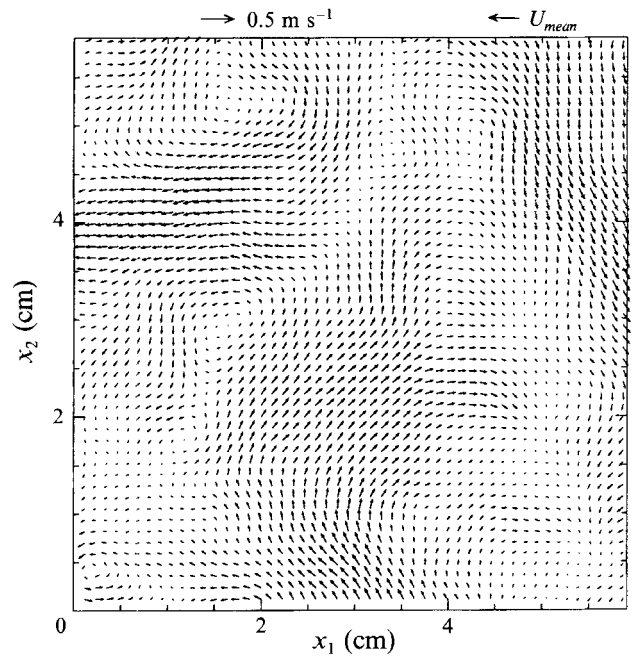

FIGURE 5. Vector map of the filtered velocity $\tilde{u}_i$. A top-hat filter was applied to the image shown in figure 2, with a width $\Delta = 8\delta \sim 48\eta$, where δ is the original grid size (0.55 mm) and η is the Kolmogorov scale. To avoid crowding, the figure shows every second vector only. The mean velocity and the fundamental velocity unit is shown on the top.

We start by assuming that a three-dimensional LES is being performed, using (for instance) a finite-volume formulation with rectangular cells. We denote the discrete LES velocity by $u_i^*(j_1,j_2,j_3)$, and assume that it represents the average velocity in the cell with centre located at $([x_1]_0+j_1\Delta_1,[x_2]_0+j_2\Delta_2,[x_3]_0+j_3\Delta_3)$. As a thought experiment, we now assume that at some instant in time the entire LES velocity field $u_i^*(j_1,j_2,j_3)$ is set equal to the real field, $\tilde{u}_i(j_1,j_2,j_3)$ which actually exists at location $([x_1]_0+j_1\Delta_1,[x_2]_0+j_2\Delta_2,[x_3]_0+j_3\Delta_3)$. The tilde denotes filtering with F_Δ, a three-dimensional top-hat filter with widths Δ_i in each direction. We now argue that in order for the LES field to continue with a realistic time evolution (i.e. for u^* to approximate $\tilde{u}$ at later times), its SGS model for the stress, $\mathscr{T}_{ij}[\boldsymbol{u}^*](j_1,j_2,j_3)$, should be equal (or as 'close' as possible) to the real stress tensor at these points, $\tau_{ij}(j_1,j_2,j_3)$.

Before proceeding with the main line of the argument, we make a connection with our present data by letting $[x_3]_0$ be the location of the data plane (with $j_3 = 0$). For simplicity, we now eliminate the reference to the x_3 direction. Furthermore, we assume that the grid resolution of the LES in the x_3 direction is very good (i.e. $\Delta_3 \sim \eta \ll \Delta$). In consequence, for the analysis of the real data we choose F_Δ to be a top-hat filter which is thin in the x_3 direction, as is effectively the case in the experiment.

Based on the data, we can evaluate the tensor $\tau_{ij}(j_1,j_2)$ as in (14). Since we are assuming that $u_i^* = \tilde{u}_i$ at the grid points (j_1,j_2), we can also compute

$$\mathscr{T}_{ij}[\boldsymbol{u}^*](j_1,j_2) = \mathscr{T}_{ij}[\tilde{\boldsymbol{u}}](j_1,j_2),$$

if a particular form of $\mathscr{T}_{ij}$ as a function of the resolved velocity field is postulated (SGS model). A simple measure of the level of agreement between τ_{ij} and $\mathscr{T}_{ij}$ is the correlation coefficient between the two fields. The reasoning which we shall adopt will

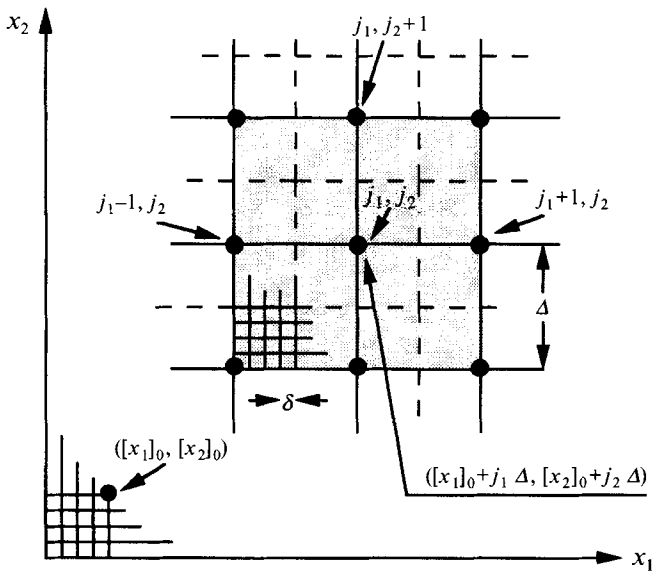

FIGURE 6. Schematic diagram showing the original grid (spacing = δ) and the coarse LES grid level (spacing = Δ). Consistent *a priori* testing requires that when comparing a model expression for the stress at point (j_1,j_2) with τ_{ij} at that same point, the model is only allowed to employ information that is available on the coarse grid (solid circles). Only after the local comparison is made, can the reference location $([x_1]_0,[x_2]_0)$ for the coarse mesh be shifted by multiples of δ to enlarge the statistical sample. The following expression is an example of box filtering at a scale 2Δ:

$$\bar{\tilde{u}}([x_1]_0+j_1\,\Delta,[x_2]_0+j_2\,\Delta) \equiv \bar{\tilde{u}}(j_1,j_2) = \tfrac{1}{4}\tilde{u}_i(j_1,j_2) + \tfrac{1}{8}\{\tilde{u}_i(j_1,j_2+1)+\tilde{u}_i(j_1,j_2-1)+\tilde{u}_i(j_1+1,j_2)+\tilde{u}_i(j_1-1,j_2)\} + \tfrac{1}{16}\{\tilde{u}_i(j_1+1,j_2+1)+\tilde{u}_i(j_1+1,j_2-1)+\tilde{u}_i(j_1-1,j_2+1)+\tilde{u}_i(j_1-1,j_2-1)\}.$$

be that the higher this correlation is, the larger will be the fraction of the flow field in which a realistic evolution of u^* can take place.

It must be stressed that the condition

$$\mathscr{T}_{ij} \approx \tau_{ij}$$

is by no means a sufficient condition for a satisfactory model, since even small errors in the model could build up and produce unrealistic results after some time. On the other hand, if a model $\mathscr{T}_{ij}$ is vastly different from τ_{ij}, then there can be little hope of capturing even the correct short-time evolution of the flow realization under scrutiny. In this sense the equality of the real and LES stress fields is a necessary, but not a sufficient condition for accurate LES prediction of a flow realization. We point out that similar arguments were made in Meneveau (1994) while dealing with statistical quantities (moments, probability densities, spectra, etc.) instead of instantaneous realizations.

Finally, we remark that the tensors $\mathscr{T}_{ij}$ and τ_{ij} could differ by a divergence-free tensor field and still have the same impact on the filtered momentum equation. For this reason we shall also compare the divergence of the tensors during the analysis.

4.3. *Consistent a priori test*

Very importantly, for the *a priori* test to be meaningful, the model stress $\mathscr{T}_{ij}$ must be evaluated based solely on the velocity field $\tilde{u}_i$ sampled on the coarse grid (of mesh size Δ). The situation is illustrated in the schematic figure 6 which shows both the original fine mesh (of spacing δ) and the coarse grid. The variable $\tilde{u}_i$ is only defined on the

coarse one (solid circles). Care must be taken not to make inadvertent use of real velocity information at smaller scales which would not be available during an actual LES. As will be seen, this could artificially raise the level of agreement between a model and the real stress. For instance, if the model $\mathscr{T}_{ij}$ involves the strain-rate tensor $\tilde{S}_{ij}$, the latter is computed from the data using centred finite differences on the coarse Δ-grid (and not on the finer measurement grid with spacing δ).

For purposes yet to be explained, we will use a second filter of characteristic size 2Δ, denoted by an *overbar*. As stated above, to maintain consistency we require that this filtering operation only use the fields as sampled on the Δ-mesh. Therefore, it is defined as follows:

$$\bar{\tilde{u}}([x_1]_0+j_1\Delta,[x_2]_0+j_2\Delta) = \sum_{m=-k}^{k}\sum_{n=-k}^{k}\beta_{m,n}\tilde{u}_i([x_1]_0+(j_1+m)\Delta,[x_2]_0+(j_2+n)\Delta) \quad \text{for} \quad j_1,j_2 \text{ even.} \tag{17}$$

This field is itself defined only on a mesh of size 2Δ. $\beta_{m,n}$ represents the discrete weights of the filter of size 2Δ. In order to obtain a filtering at scale 2Δ which resembles a top-hat filter and which is centred around the node (j_1,j_2), one can choose the following weights: $\beta_{0,0}=\frac{1}{4}$, $\beta_{0,1}=\beta_{1,0}=\beta_{0,-1}=\beta_{-1,0}=\frac{1}{8}$ and $\beta_{1,1}=\beta_{-1,-1}=\beta_{1,-1}=\beta_{-1,1}=\frac{1}{16}$. These weights mimic a uniform average over the shaded area of size 2Δ shown in figure 6. The fact that this second filtering is not precisely a top-hat filter does not pose any serious difficulties, since the relevant feature of the analysis is that one must be able to perform the filtering solely in terms of the resolved data.

For the Gaussian filter, the $\beta_{m,n}$ decay at a prescribed rate,

$$\beta_{m,n} = K\,\mathrm{e}^{-6(m^2+n^2)/4}, \tag{18}$$

and the sum is extended over all available points. The coefficient K normalizes the discrete filter. For the cut-off filter, we use

$$\beta_{m,n} = K\frac{\sin(\frac{1}{2}\pi m)}{\frac{1}{2}\pi m}\frac{\sin(\frac{1}{2}\pi n)}{\frac{1}{2}\pi n}. \tag{19}$$

Analogous definitions are employed to define a filter of size 4Δ, which will be denoted by a *hat*. It is defined on a mesh of size 4Δ and is computed only based on the values of the *overbar* field on the mesh of size 2Δ.

4.4. *Correlation between SGS stress and stain rate*

Here we wish to examine the degree to which eddy-viscosity closures represent the local and instantaneous stress. As outlined in §4.2, this can be quantified by measuring the correlation coefficient between the real and the modelled stress. The correlation coefficient between two variables a and b is defined in the usual way,

$$\rho(a,b) \equiv \frac{\langle ab\rangle-\langle a\rangle\langle b\rangle}{[(\langle a^2\rangle-\langle a\rangle^2)(\langle b^2\rangle-\langle b\rangle^2)]^{1/2}}. \tag{20}$$

In order to evaluate the Smagorinsky model

$$\mathscr{T}_{ij}^{(S)} = -2(c_s\Delta)^2[2\tilde{S}_{pq}\tilde{S}_{pq}]^{1/2}\tilde{S}_{ij}, \tag{21}$$

we need to compute the local filtered rate-of-strain magnitude $|\tilde{S}| = (2\tilde{S}_{pq}\tilde{S}_{pq})^{1/2}$. From the data we have $\tilde{S}_{11}$, $\tilde{S}_{22}$, $\tilde{S}_{33}=-(\tilde{S}_{11}+\tilde{S}_{22})$ and $\tilde{S}_{12}$. An approximation must be made for the $\tilde{S}_{13}$ and $\tilde{S}_{23}$ elements (which cannot be measured from our data). We assume that $\tilde{S}_{23}=\tilde{S}_{13}=\tilde{S}_{12}$. While we do not expect the errors associated with this

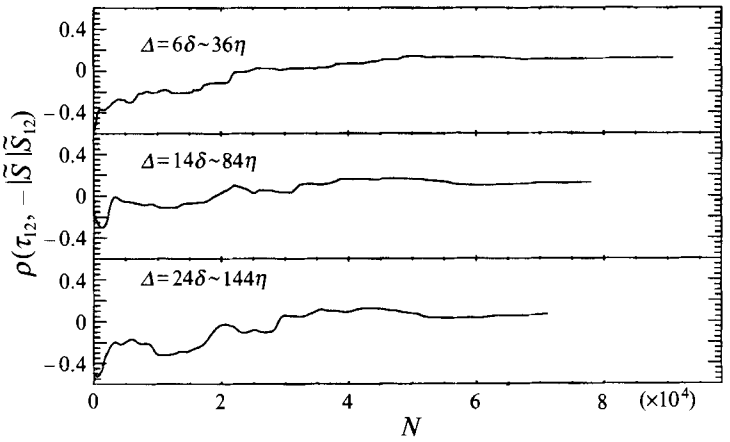

FIGURE 7. Correlation coefficients between τ_{12} and $-|\tilde{S}|\,\tilde{S}_{12}$, where an increasing number of points N are used to compute the averages.

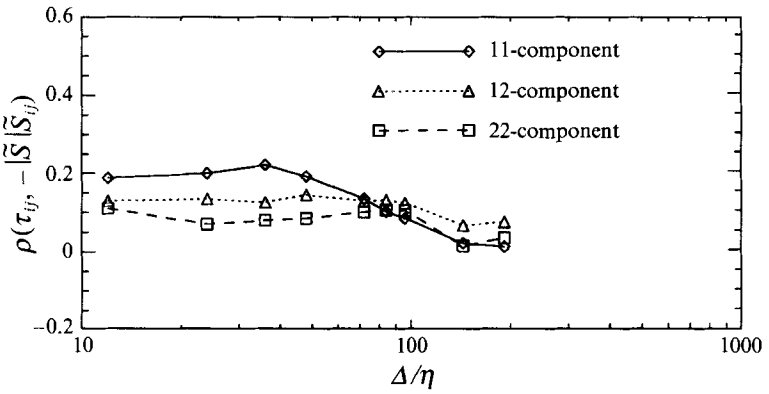

FIGURE 8. Correlation coefficients between elements of τ_{ij} and $-|\tilde{S}|\,\tilde{S}_{ij}$ as function of filter width Δ (top-hat filter) for different tensor components.

approximation to significantly influence the resulting correlation coefficients, we take the opportunity to stress that this is really an assumption that should, ultimately, be re-examined with more detailed measurements of all velocity components and strain-rate elements.

The averaging is done over $[128(L-\Delta)/L]^2$ points ($L = 7$ cm) and over six images, for each tensor element (1, 1), (1, 2), and (2, 2). Strictly speaking, one should compare only the deviatoric part of τ_{ij} to the Smagorinsky prediction. We cannot do this, however, since we are not measuring the u_3 component. While the approximation could affect the results for the (1, 1) and (2, 2) components, it does not affect those of the (1, 2) component.

The test is a consistent one because the strain rate is computed only from the data available at the coarse mesh. Statistical convergence of the correlation coefficient $\rho(\tau_{ij}, \mathscr{T}_{ij}^{(S)})$ is good, as seen from the running averages plotted in figure 7. The results are shown in figure 8, as a function of filter width Δ. As can be seen, the level of correlation is quite low, between 0 and 0.2. Similar values are obtained for all filter types. Similarly small correlation coefficients are found for other eddy-viscosity models (where the eddy viscosity is given in terms of the vorticity magnitude, subgrid kinetic energy, etc.),

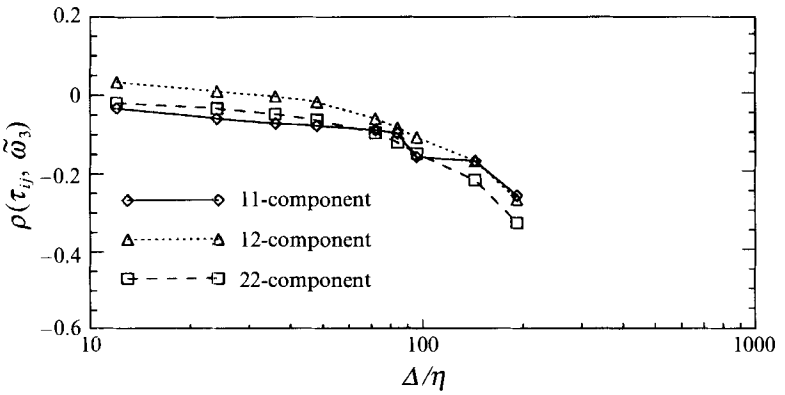

FIGURE 9. Correlation coefficients between elements of τ_{ij} and the resolved vorticity component $\tilde{\omega}_3$, as function of filter width Δ (top-hat filter).

essentially because there is no alignment between the tensors τ_{ij} and $\tilde{S}_{ij}$ in the first place. These results are entirely consistent with numerous previous findings based on DNS data, only that now they are confirmed for turbulence at considerably higher Reynolds number.

For completeness, we also present correlation coefficients between τ_{ij} and the resolved vorticity component in the x_3 direction. The results are shown in figure 9. As can be seen, the correlation is also low, not exceeding 0.2 in magnitude except at the largest scale. However, one should not conclude that vorticity is unimportant, since in §7, we shall find other more detailed relationships between stresses and the entire velocity gradient tensor, which includes the vorticity.

The results of this section serve as motivation to search for improved SGS modelling, that hopefully should display better agreement with the real stress. A starting point for this search is to observe the rate at which the real stresses dissipate resolved kinetic energy and how this energy flux is distributed amongst the small scales. The next two sub-sections focus on these questions.

4.5. *Energy flux to subgrid scales*

The energy flux to unresolved scales is defined as follows:

$$\Pi(\Delta) = -\tau_{ij}\tilde{S}_{ij}, \tag{22}$$

and one expects its (ensemble) average to be of the same order of magnitude as the dissipation rate ϵ in this near-equilibrium flow. To ascertain if this is the case for the present data, we compute the average of $\Pi(\Delta)$ over the six images (i.e. a combination of spatial and ensemble averaging), for a range of filter sizes Δ. Since not all tensor elements entering the contraction on the right-hand side of (22) are being measured, some approximations must be made. In particular, we assume that $\langle\tau_{13}\tilde{S}_{13}\rangle = \langle\tau_{23}\tilde{S}_{23}\rangle = \langle\tau_{12}\tilde{S}_{12}\rangle$ and that $\langle\tau_{33}\tilde{S}_{33}\rangle = \langle\frac{1}{2}(\tau_{11}+\tau_{22})\tilde{S}_{33}\rangle$. After using the incompressibility condition to evaluate $\tilde{S}_{33}$ one obtains

$$\langle\Pi(\Delta)\rangle \approx -\tfrac{1}{2}(\langle\tau_{11}\tilde{S}_{11}\rangle + \langle\tau_{22}\tilde{S}_{22}\rangle - \langle\tau_{11}\tilde{S}_{22}\rangle - \langle\tau_{22}\tilde{S}_{11}\rangle + 12\langle\tau_{12}\tilde{S}_{12}\rangle). \tag{23}$$

While this expression would be exact for isotropic turbulence, we have found that isotropy conditions are not met among the terms that we can measure. However, since we shall focus on trends and not on exact numerical values of the energy flux, we proceed with our present approximations.

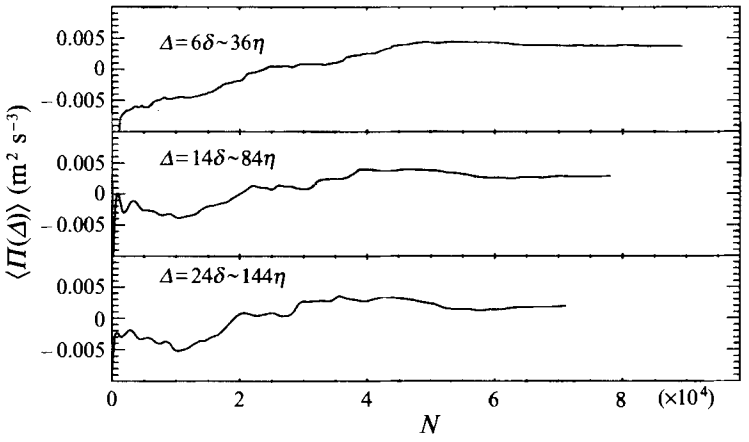

FIGURE 10. Running average ($\Sigma_N(\Pi)/N$) of the SGS energy flux as function of number of data points N employed to compute the average. The top-hat filter is used.

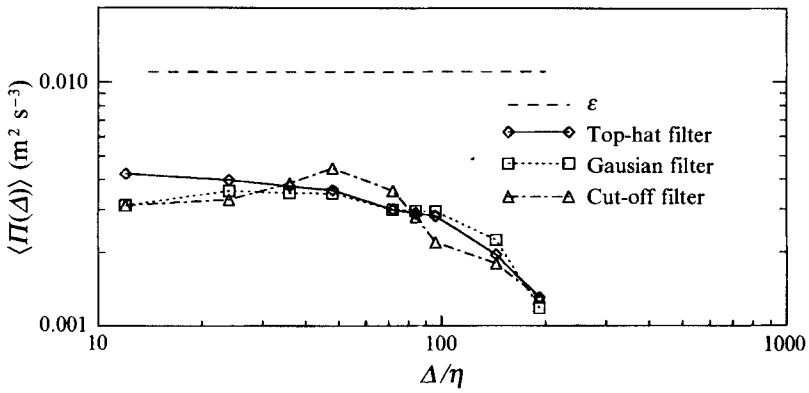

FIGURE 11. Symbols: average subgrid-scale energy flux $\langle \Pi(\Delta) \rangle$ as function of filter size Δ, for the top-hat filter. As a reference, the horizontal dashed line represents the large-scale estimate for the overall rate of dissipation $\epsilon \approx u'^3/l \sim 0.011\ \mathrm{m^2/s^{-3}}$.

When computing the average value of $\Pi(\Delta)$, statistical convergence is of concern, since we are dealing with a third-order moment of the velocity. Such moments are known to converge very slowly. In figure 10 we show running averages of $\Pi(\Delta)$ as a function of the number of points employed in the calculation, for several values of Δ. As can be seen, this statistic is quite slow in converging and some oscillations are visible even after analysing six images. Since other statistical features of interest in this study (such as correlation coefficients) display better convergence, we proceed with six images but refrain from ascribing too much significance to the numerical value encountered for $\langle \Pi(\Delta) \rangle$. In figure 11, this flux is plotted as a function of the filter width Δ, for the three filter types considered. It is apparent that $\langle \Pi(\Delta) \rangle$ is not very sensitive to the filter type, and that its value is of the same order of magnitude as ϵ, over a range of Δ-values. Better agreement need not be expected since the estimate of ϵ is itself an *ad hoc* order-of-magnitude approximation based on the large-scale rate of injection of energy. We conclude that the data exhibit the flow structures and subtle phase coherencies that are required for the classical cascade of energy to be taking place.

Another quantity that is indicative of energy transfer, the third-order velocity structure function, did not exhibit satisfactory statistical convergence over the six

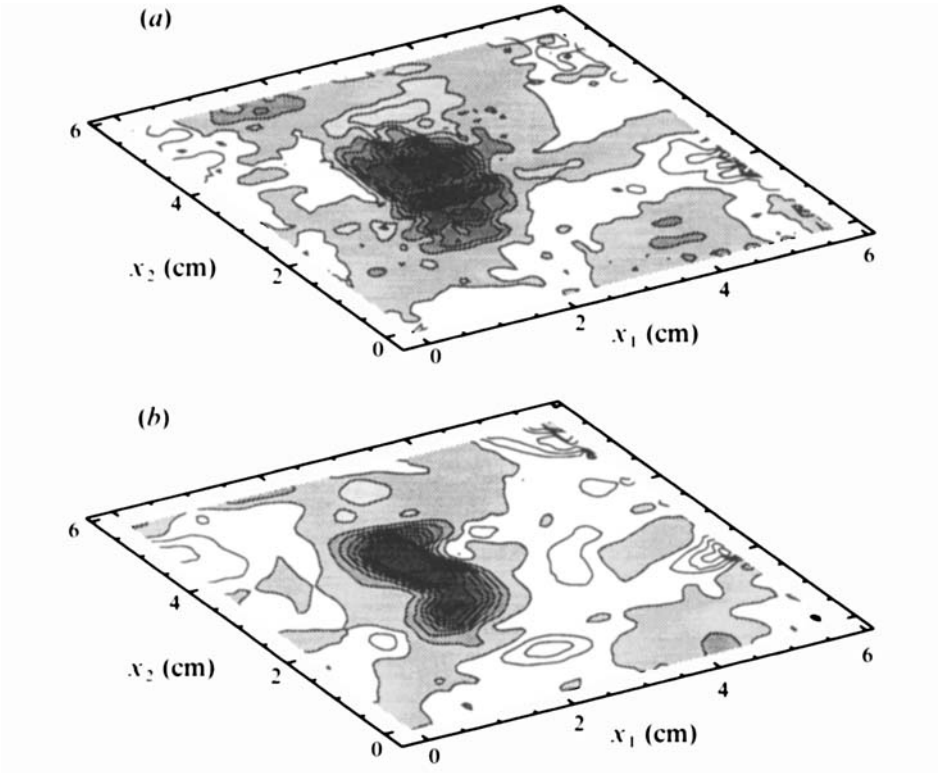

FIGURE 12. Contour plots of spatial distribution of energy flux, for the top-hat filter. (*a*) The ('not-so-local') flux $\bar{\tau}_{pq}\bar{\bar{S}}_{pq}$, going from scales above 2Δ to all scales smaller than Δ. (*b*) $L_{pq}\bar{\bar{S}}_{pq}$, the 'local' flux of energy that goes from scales larger than 2Δ to scales between Δ and 2Δ. Darkest grey corresponds to a value of $0.048\ \mathrm{m^2\,s^{-3}}$, and the contours are spaced by constant increments of $-0.006\ \mathrm{m^2\,s^{-3}}$. White regions denote negative values.

images. More data will have to be analysed in order to obtain that variable reliably. On the other hand, the velocity-derivative skewness cannot be evaluated from these data since the dissipation range is not resolved.

4.6. *Energy flux at a larger scale*

As a next step, we wish to study the flux of energy that goes to all scales smaller than 2Δ. We use a definition slightly different from that of $\Pi(\Delta)$, namely a *consistent* definition as far as LES on a grid with mesh size Δ is concerned. We define this flux as

$$\Pi^*(2\Delta) = -T_{pq}\bar{\bar{S}}_{pq}, \tag{24}$$

where

$$T_{ij} = \widetilde{\bar{u}_i\bar{u}_j} - \tilde{\bar{u}}_i\tilde{\bar{u}}_j. \tag{25}$$

Here the *overbar* variables are computed based only on the *tilde* variables at the discrete Δ-mesh points, as discussed in §4.2.

Next, we recall the Germano identity (Germano 1992) and recognize that $\Pi^*(2\Delta)$ consists of two contributions,

$$\Pi^*(2\Delta) = -(L_{pq}\bar{\bar{S}}_{pq} + \bar{\tau}_{pq}\bar{\bar{S}}_{pq}). \tag{26}$$

The resolved stress L_{ij} is defined as

$$L_{ij} = \widetilde{\bar{u}_i\bar{u}_j} - \tilde{\bar{u}}_i\tilde{\bar{u}}_j, \tag{27}$$

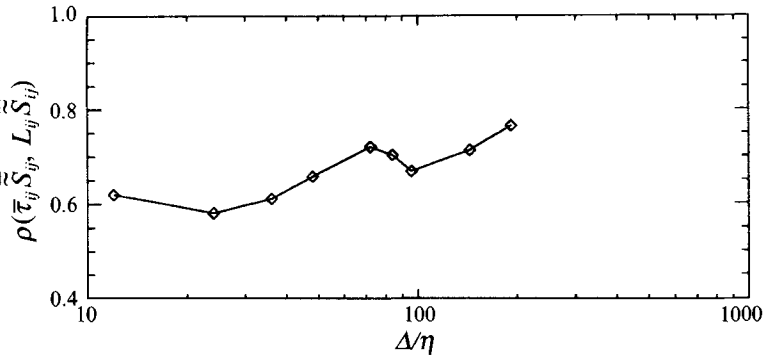

FIGURE 13. Correlation coefficients between $L_{pq}\bar{\bar{S}}_{pq}$ and $\bar{\tau}_{pq}\bar{\bar{S}}_{pq}$ as a function of Δ, for the top-hat filter.

and it will later be found to have substantial significance. The first term $L_{pq}\bar{\bar{S}}_{pq}$ can be interpreted as the energy flux from large scales to scales of sizes in between Δ and 2Δ (we shall refer to it as the 'local' contribution). The second term $\bar{\tau}_{pq}\bar{\bar{S}}_{pq}$ corresponds to the energy flux to scales smaller than Δ (referred to as 'not-so-local' contribution, because the scale disparity is larger than a factor of two).

In order to evaluate the two flux contributions from the data, we employ the approximations of (23), but without the averaging. It must be recognized that the present approximation is less justified than that of (23), since it is now invoked for the instantaneous values. We must postulate that the overall trends that are observed are not influenced too strongly by this approximation. Figure 12 shows contour plots of $L_{pq}\bar{\bar{S}}_{pq}$ and of $\bar{\tau}_{pq}\bar{\bar{S}}_{pq}$, for the top-hat filter and for $\Delta = 8\delta \sim 48\eta$. At each point, the sum of both quantities yields $\Pi^*(2\Delta)$. According to the discussion in §4.2, these variables are defined on a coarser grid $([x_1]_0 + 2j_1\Delta, [x_2]_0 + 2j_2\Delta]$. Nevertheless, a smooth field can be obtained (for plotting purposes) by sliding the reference point $([x_1]_0, [x_2]_0)$ inside the initial coarse box, centred at $(j_1 = 0, j_2 = 0)$.

A crucial observation is that coarse features of the two flux contributions appear to be reasonably well correlated among themselves (for the image shown, the correlation coefficient is $\rho = 0.68$). To better quantify this observation, the correlation coefficient between the two fluxes is computed over all six images. The averaging is performed over all points on the coarse grid, as well as over all possible reference points $([x_1]_0, [x_2]_0)$ inside the initial coarse box. Figure 13 shows the correlation coefficient between $L_{pq}\bar{\bar{S}}_{pq}$ and $\bar{\tau}_{pq}\bar{\bar{S}}_{pq}$, as a function of Δ (top-hat filter). As can be seen, it is a substantial correlation. That is to say, whenever there is, for example, a large value of $\Pi(2\Delta)$, it is most often distributed in such a way that both the 'local' and the 'not-so-local' parts of the flux are large. Or, if there is backscatter of energy at the large scale ($\Pi(2\Delta) < 0$), it appears more likely that both the 'local' and the 'not-so-local' parts exhibit backscatter. In the next section, we will study the flow field itself to find the basis for this correlation, and we will explore its implications for SGS modelling.

5. The scale similarity of the velocity field

In the last section we found considerable resemblance of both the contractions of L_{ij} and $\bar{\tau}_{ij}$ with the large-scale rate of strain. This observation must have its roots in some similarity that exists between flow features that govern the tensors L_{ij} and $\bar{\tau}_{ij}$. In fact, we focus directly on tensors L_{ij} and τ_{ij}, which is where our ultimate interest lies.

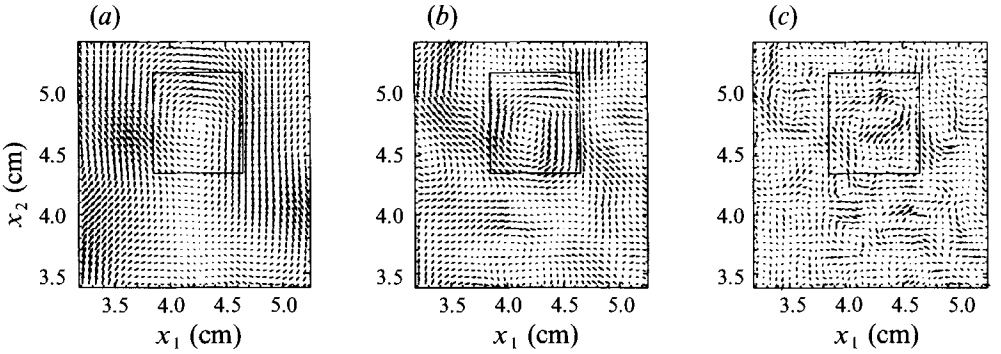

FIGURE 14. Velocity maps in consecutive bands, of characteristic scale $L/2^n$ (where L = size of entire image). From (*a*)–(*c*): $n = 3, 4, 5$. The bands are defined as the difference between two low-pass-filtered versions of the velocity field. Larger-scale fields are sampled on coarser grids that properly emulate the information available during LES. Bilinear interpolation is used to generate smooth fields, for graphical purposes. To avoid crowding, only a subset of an image is shown. Some similar features in vortical regions can be recognized in consecutive bands.

5.1. *The velocity field decomposed into bands*

It is useful to separate the data into different scales of motion ('bands'). This decomposition facilitates the identification of flow features that dominate events close to the cut-off Δ of interest. We now decompose the fluctuating velocity field $u_i(x)$ into contributions from separate bands, according to

$$u_i(x) = \sum_{n=1}^{N} u_i^{(n)}(x), \tag{28}$$

where the velocity field in each band is given by

$$u_i^{(n)}(x) = \tilde{u}_i(x) - \bar{u}_i(x). \tag{29}$$

The *tilde* represents top-hat filtering at a scale $\Delta = 2^{-n}L$ while the *overbar* also represents low-pass filtering, but at a larger scale $2^{-(n-1)}L$. However, in order to assure that no trivial overlap of information between bands is generated, we must again be careful how these data are sampled. For the *tilde* operation we use sampling on a grid of size Δ. Then some known (e.g. bilinear) interpolation scheme is employed to generate a 'smooth' field in between those points, for graphical illustration purposes. The *overbar* operation only uses information that is available on the Δ-grid and is itself sampled on a grid of spacing $2\Delta = 2^{-(n-1)}L$. Again, a smooth field is generated by (bilinear) interpolation. The band-velocity $u_i^{(n)}(x)$ is the difference between the two smooth fields, each of which has been constructed only with discrete information available at the previous step.

5.2. *The scale coherence of flow structures*

From our data set, we consider three bands ranging from $n = 3$ to $n = 5$ (while $N = 7$). Figure 14 shows samples of the vector fields $u_i^{(n)}$. For clarity, only small subsets of the entire vector fields are shown. If we focus attention on the highlighted regions, we notice some similarity between (sections of) vortex-like flow structures that exist in consecutive bands, at about the same locations. Some streaming regions also display similarity. We have made similar observations based on the other images. Of course, the similarity does not extend to the entire flow field, as the smaller-scale bands contain

more structures with no counterparts at the large scales. For instance, the lower-right corners in the vector maps for $n = 3$ and $n = 4$ (figure 15) exhibit distinctly different flow features.

Two physical interpretations for this partial scale coherence can be ventured. The first involves the concept of the energy cascade, in the following sense: small eddies (in band $n+1$) have some history in common with the larger eddies (in band n). They have both been influenced by the even bigger eddies (from band $n-1$), during some time interval. Although by classical arguments one expects that the strongest influence on band $n+1$ comes from band n, some influence from band $(n-1)$ is still felt by band $n+1$ ('not-so-local' interactions). Thus the 'effective forcing' of bands n and $n+1$ due to band $n-1$ has some degree of similarity. Therefore, it is plausible that their response (the resulting velocity field) may also show some common features. A second interpretation can be given in terms of coherent structures: clearly, a physically meaningful flow structure needs information from several bands (unless one defines the bands using a filter which is exactly parallel (in function space) to the structure itself). If a given structure is decomposed into bands, the correlation may arise because one is really looking at the same single structure. Both interpretations may in fact be related, or complementary. For now, we use the observations for modelling purposes.

5.3. *Relation between SGS stress and velocity bands*

Now that we have qualitatively shown some resemblance between the velocities in successive bands, a connection must be found between them and the SGS stress τ_{ij}. Using the usual scaling arguments one can argue that the SGS stress is dominated by the largest unresolved scales. In other words, if we select $\Delta = 2^{-n}L$, then τ_{ij} should be dominated by $u_i^{(n+1)}$. This argument is not complete, however, owing to the known large-scale contribution to the SGS stress which appears through the Leonard stress and the cross-stress (Leonard 1974). Therefore, to approximate the SGS stress one should at least keep the last resolved band (n) and the first unresolved one ($n+1$) as follows:

$$\tau_{ij}^{(n)} = \widetilde{(u_i^n + u_i^{n+1})(u_j^n + u_j^{n+1})} - \widetilde{(u_i^n + u_i^{n+1})}\,\widetilde{(u_j^n + u_j^{n+1})}. \tag{30}$$

The tilde represents, as before, filtering at scale Δ of the entire expression contained below the bracket. Figure 15 shows contour plots of the band-approximated stress element $\tau_{12}^{(n)}(x)$ and the real stress $\tau_{12}(x)$, for $\Delta = 2^{-3}L$ ($n = 3$). The latter variable has been constructed in a similar way: by sampling on a grid of mesh size Δ coincident with the grid used to generate $\tau_{12}^{(n)}(x)$, and using bilinear interpolation. As can be seen, the representation in terms of two bands surrounding the cut-off scale is quite satisfactory. The correlation coefficient between each element $\tau_{ij}^{(n)}$ and τ_{ij} is typically close to 0.83.

As a parenthetical disgression, we remark that (30) can be written as

$$\tau_{ij}^{(n)} = \mathscr{R}_{ij}^{(n)} + \mathscr{C}_{ij}^{(n)} + \mathscr{L}_{ij}^{(n)}, \tag{31}$$

where

$$\mathscr{R}_{ij}^{(n)} = \widetilde{u_i^{n+1} u_j^{n+1}} - \widetilde{u_i^{n+1}}\,\widetilde{u_j^{n+1}}$$

is akin to a SGS Reynolds stress which involves only the small scales,

$$\mathscr{C}_{ij}^{(n)} = (\widetilde{u_i^{n+1}}\,\widetilde{u_j^n} - \widetilde{u_i^{n+1}}\,\widetilde{u_j^n}) + (\widetilde{u_i^n u_j^{n+1}} - \widetilde{u_i^n}\,\widetilde{u_j^{n+1}})$$

is a cross-stress, while

$$\mathscr{L}_{ij}^{(n)} = \widetilde{u_i^n u_j^n} - \widetilde{u_i^n}\,\widetilde{u_j^n}$$

resembles a Leonard stress involving solely the resolved scales. Each of these expressions is Galilean invariant, as opposed to the definitions usually employed, for

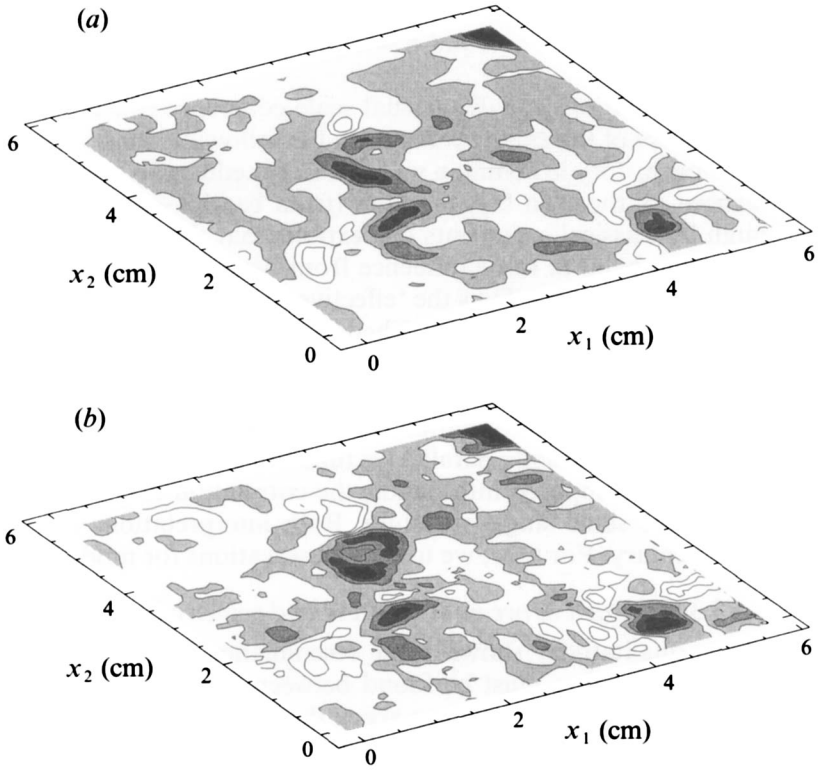

FIGURE 15. (*a*) Contour plot of the real SGS stress element τ_{12}, computed with a top-hat filter of width $\Delta = 2^{-3}L$. Contours range from $-0.0048\ \mathrm{m^2\,s^{-2}}$ (dark) to $0.00288\ \mathrm{m^2\,s^{-2}}$, at intervals of $0.00096\ \mathrm{m^2\,s^{-2}}$. (*b*) Contour plot of $\tau_{12}^{(n)}$, the SGS stress estimated from the velocity field in the two bands surrounding the scale Δ. Contours range from $-0.002\ \mathrm{m^2\,s^{-2}}$ (dark) to $0.002\ \mathrm{m^2\,s^{-2}}$, at intervals of $0.0005\ \mathrm{m^2\,s^{-2}}$.

which the cross-stresses do not have this property. In this regard these expressions mirror the elegant decomposition proposed some time ago by Germano (1986).

6. The stress-similarity model

The basic observation of similarity between the vector fields $u_i^{(n+1)}$ and $u_i^{(n)}$ (and between $u_i^{(n)}$ and $u_i^{(n-1)}$) means that there is some similarity between $\tau_{ij}^{(n)}$ and $\tau_{ij}^{(n-1)}$. We have already shown that $\tau_{ij}^{(n)}$ is a good approximation for the real SGS stress τ_{ij}. A further approximation that simplifies the formulation is to rewrite $\tau_{ij}^{(n-1)}$ in terms of the band velocities, and use (29). One obtains

$$\tau_{ij}^{(n-1)} = \overline{(\tilde{u}_i - \hat{u}_i)(\tilde{u}_i - \hat{u}_i)} - \overline{(\tilde{u}_i - \hat{u}_i)}\ \overline{(\tilde{u}_j - \hat{u}_j)}, \tag{32}$$

where the *hat* signifies further filtering of the *overbar* data at a scale $4\Delta = 2^{-(n-2)}L$. Since $\hat{u}$ is almost constant over distances of 2Δ, we can approximate products involving $\hat{u}_i$ as $\overline{\tilde{u}_i \hat{u}_j} \approx \bar{\tilde{u}}_i \bar{\hat{u}}_j$. It leads to a cancellation of $\hat{u}_i$ and yields $\tau_{ij}^{(n-1)} \approx L_{ij}$. Finally, these considerations imply that there must be some similarity between τ_{ij} and L_{ij}. If no better information is available, it would appear that a 'best guess' for the SGS stress is to set it to be proportional to L_{ij}. Finally, the proposed stress-similarity model reads

$$\mathscr{T}_{ij} = c_L L_{ij}. \tag{33}$$

The stress L_{ij} can be entirely computed from the resolved velocity at the LES grid points; c_L is a dimensionless model coefficient yet to be specified (see §9).

A comparison among τ_{12}, L_{12} and the Smagorinsky prediction $\mathscr{T}_{12}^{(S)} = -2(c_s \Delta)_2 |\tilde{S}| \tilde{S}_{12}$ is presented by the colour contour maps in figure 16. As explained before, we have computed τ_{12} at points $\boldsymbol{x}$, while computing L_{12} and $\tilde{S}_{ij}$ by only employing the (discrete) data $\tilde{u}_i(x_1 + m\Delta, x_2 + n\Delta)$. However, a smooth contour plot is produced by varying $\boldsymbol{x}$ along the original fine mesh. The vector maps represent the velocity fields on which these tensors depend most strongly, namely the fields in bands $n = 4$ and $n = 3$, respectively. The filter size is $\Delta = 8\delta \sim 48\eta$ and a top-hat filter has been used. It is evident that the agreement between τ_{12} and the stress-similarity model is significantly better than between τ_{12} and the Smagorinsky model. One important distinction between L_{12} and τ_{12} is that the fluctuations of L_{12} occur over bigger lengthscales than those of τ_{12}. This discrepancy is due to the fact that the former is dominated by the unresolved scales of motion $\boldsymbol{u}^{(n+1)}$ (shown by the vectors in figure 16*a*), while those of L_{ij} are dominated by the resolved velocity field $\boldsymbol{u}^{(n)}$ (shown by the vectors in figures 16*b* and 16*c*). The similarity between the vector fields $\boldsymbol{u}^{(n+1)}$ and $\boldsymbol{u}^{(n)}$ described before can be also observed here.

Next, the correlation coefficients between components of L_{ij} and τ_{ij} are computed, as a function of Δ. Figure 17 shows the results, for the top-hat filter. The values corresponding to Δ above 100η display some scatter. This could be due to a lack of convergence, given our limited data base (especially at large scales), or to a possible lack of similarity at the large-scale end of the inertial range. However, we find that the correlation coefficients for smaller Δ appear well converged (see running averages plotted in figure 18). The overall degree of correlation is substantially higher than for the Smagorinsky model, as can be seen by comparing figure 18 with figure 7. Also, this result is relevant to LES because a consistent *a priori* test has been employed and no small-scale information has been used in a fashion which is inconsistent with LES. To clearly drive home this last point, we exemplify how one can obtain a higher correlation coefficient if the *a priori* analysis is not consistent. Suppose that we had defined the *overbar* filter in the same fashion as the *tilde* filter, namely as a filter of scale 2Δ acting on the data at the original fine grid (δ). The correlation between τ_{ij} and L_{ij} computed in this fashion is considerably larger, between 0.7 and 0.8. The reason is that L_{ij} now contains small-scale information not available during LES.

6.1. *Influence of filter type*

We repeat the calculations of τ_{ij} and L_{ij}, now using the Gaussian filter. Again, the second filtering is done in a consistent fashion, using only the *tilde* field on a coarse grid. The resulting correlations are comparable to those of the top-hat filter (see figure 19). Nevertheless, if the procedure is repeated using the cut-off filter, the correlation is very low (see bottom curves in figure 19). This result is consistent with the findings of Meneveau, Lund & Moin (1992) who, based on DNS data at low Reynolds numbers, analysed the correlation between L_{ij} (proposed then only as a surrogate for the Bardina model) and τ_{ij}, using the cut-off filter. They obtained negligible correlation.

We come to the conclusion that the subtle similarity between scales needs a filtering (and discretization) with enough localization in physical space in order to be discernible. Our results show that the cut-off filter induces too many oscillations in physical space, and as a consequence the correlation between local flow features is lost.

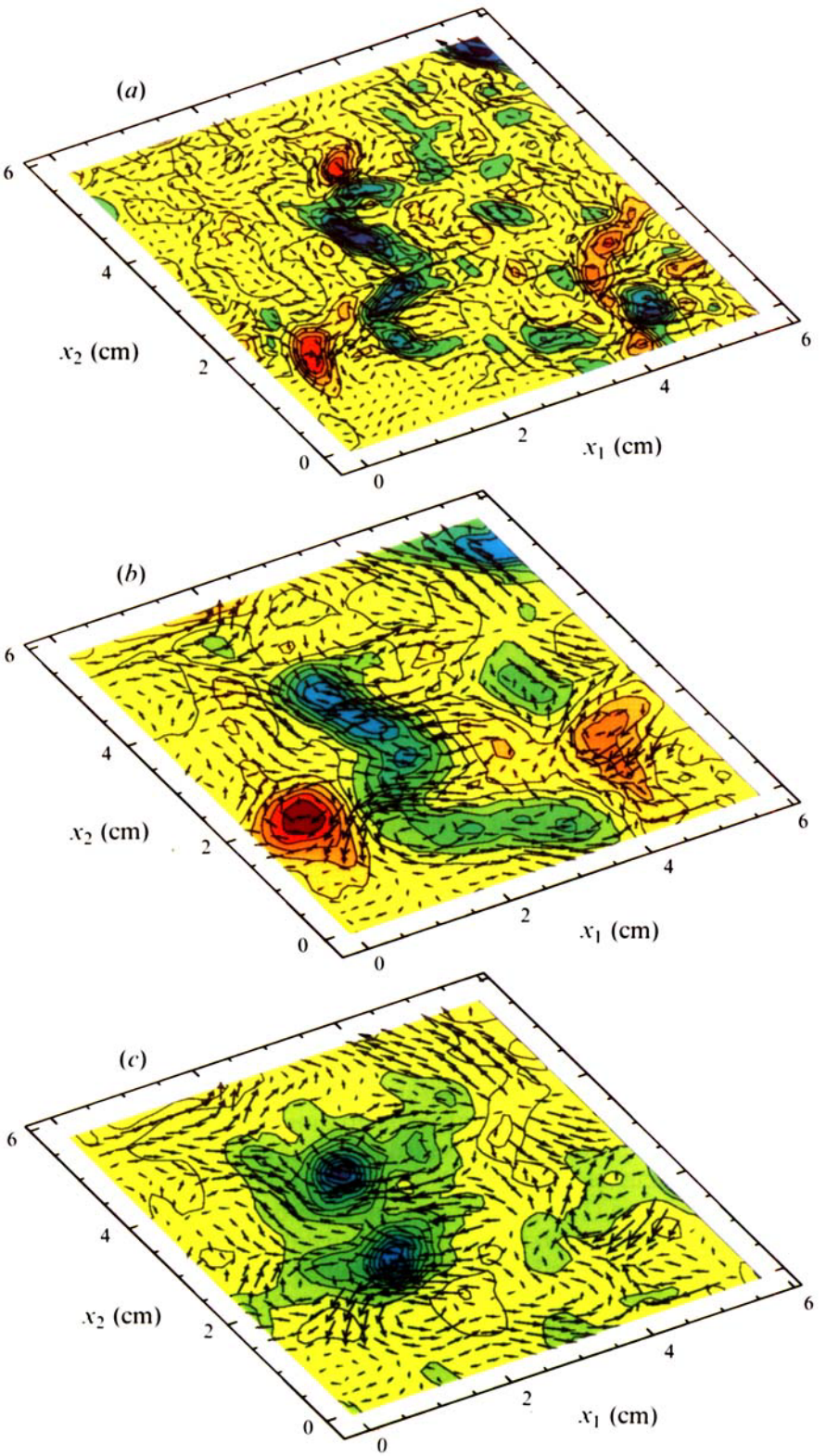

FIGURE 16. For caption see facing page.

6.2. *Comparison with the Bardina model*

As outlined in the introduction, the first similarity model was proposed by Bardina *et al.* (1980). It involves a second filtering at the grid-level scale Δ, as opposed to the scale 2Δ used to calculate L_{ij}. We have repeated the consistent *a priori* test for the Bardina model. Usually, the Bardina model is used in conjunction with the Gaussian filter, which puts some weighting on all points of the Δ-grid. However, we notice that the weights of even the closest points are very small compared to the central point (their ratio is exp (6) $\sim$ 400!). The consequence is that the fluctuations of $\mathscr{T}_{ij}^{(B)}$ are very weak. We have measured the r.m.s. level of τ_{ij} and that of $\mathscr{T}_{ij}^{(B)}$ from the data, at $\Delta = 14\delta$. We find the former to be $\sigma_\tau \sim 1.4 \times 10^{-3}$ m^2 s^{-2}, while the second is $\sigma_B \sim 6 \times 10^{-5}$ m^2 s^{-2}. This disparity in intensity means that the model has little influence on the simulation, unless it is multiplied by a very large model coefficient. On the other hand, the low-intensity fluctuations of $\mathscr{T}_{ij}^{(B)}$ do display some similarity with those of τ_{ij}. The corresponding correlation coefficients are only marginally lower ($\rho(\tau_{ij}, \mathscr{T}_{ij}^{(B)}) \sim 0.5$–$0.55$) than those of L_{ij}. We may point out that in the past (Bardina *et al.* 1980, etc.), this model was reported to have much higher correlation ($\rho \sim 0.8$). We have repeated the *a priori* test in the traditional fashion, i.e. with a second filtering based on the fine-grained data (where $\tilde{u}_i$ is employed at all grid points of the δ-mesh when computing the second filtering). Then the result is $\rho \sim 0.85$, which is quite comparable to the earlier results based on DNS *a priori* testing. However, we argue that such a high correlation is an artifact of using information that is unavailable during LES.

In spite of this 'critique' of the initial formulation of the similarity model, it is highly encouraging to find that the correlation of the revised model is still substantially higher than that of the Smagorinsky model. The basic physical ideas that underlie the approach originally proposed by Bardina *et al.* (1980) appear hereby corroborated from the consistent *a priori* test applied to the experimental data.

6.3. *Analysis of synthetic fields*

Another question which, for completeness, we would like to address is the following: What correlations are obtained when analysing random, non-turbulent fields? With such a question we mean to verify that the correlations observed between τ_{ij} and L_{ij} are a result of physical processes and not some artifact which may be valid for any type of signals. For this purpose, we generated velocity fields consisting of random numbers (white noise). Each velocity component is generated independently, and a total of six 'images' consisting of 128×128 random vectors are considered. One would not expect to find correlations between τ_{ij} and L_{ij} for this type of data. In fact, one obtains values that are almost zero (see figure 20 where a running average is presented, for $\Delta = 14\delta$ and a top-hat filter). The slight deviation from zero is because statistical convergence is not complete.

FIGURE 16. (*a*) Contour plot of the real SGS stress element τ_{12} computed with a top-hat filter. The filter size is in the inertial range ($\Delta = 8\delta \sim 48\eta$; δ = measurement grid size, η = Kolmogorov scale). Contour levels range from dark blue ($\tau_{12} = -4.8 \times 10^{-3}$ m^2 s^{-2}) to red ($\tau_{12} = 2.9 \times 10^{-3}$ m^2 s^{-2}), in increments of 0.64×10^{-3} m^2 s^{-2}. The vectors represent the largest of the 'unresolved' velocity field $\boldsymbol{u}^{(n+1)}$. A vector length of 1 cm (in units of the figure) corresponds to a velocity of 0.22 m s^{-1}. (*b*) Contour plot of L_{12}, the stress computed based on the resolved velocity field. For a discussion on the consistent sampling procedure used, see text. Contour levels range from dark blue ($L_{12} = -3.2 \times 10^{-3}$ m^2 s^{-2}) to red ($L_{12} = 2.7 \times 10^{-3}$ m^2 s^{-2}), in increments of 0.5×10^{-3} m^2 s^{-2}. The vectors represent the smallest scales of the resolved velocity field, $\boldsymbol{u}^{(n)}$ (same units as in (*a*)). (*c*) Contour plot of $\mathscr{T}_{12}^S = -|\tilde{S}|\,\tilde{S}_{12}$, the prediction of the Smagorinsky model (without the model constants). Contour levels range from dark blue ($\mathscr{T}_{12}^S = -1025$ s^{-2}) to red ($\mathscr{T}_{12}^S = 355$ s^{-2}), in increments of 110 s^{-2}. As above, the vectors represent $\boldsymbol{u}^{(n)}$ which contributes mostly to $\tilde{S}_{ij}$.

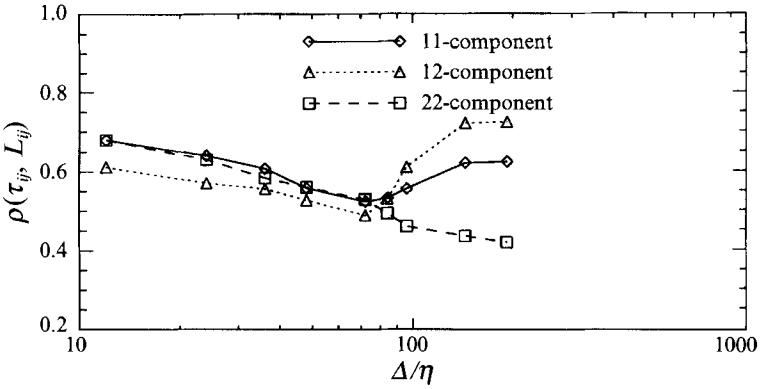

FIGURE 17. Correlation coefficients between τ_{ij} and L_{ij} as function of filter width (top-hat filter), for different tensor elements.

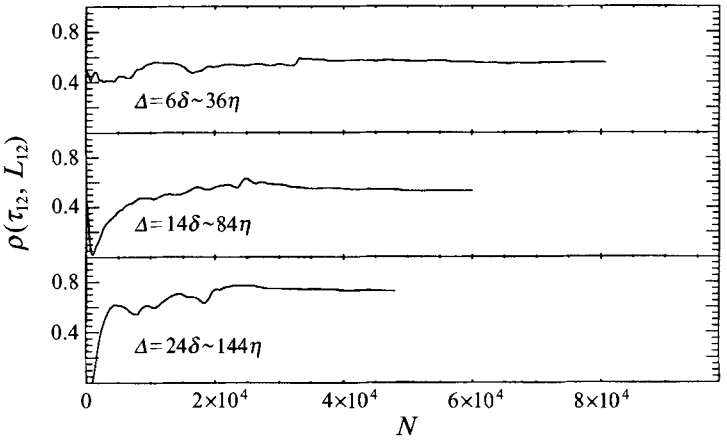

FIGURE 18. Running averages of the correlation coefficients between τ_{12} and L_{12}, as function of the number of points employed for the averaging.

Of more physical interest is the behaviour of the (τ_{ij}, L_{ij}) correlation for random data with a more realistic energy spectrum. A synthetic velocity field v_i with a $-\frac{5}{3}$ spectrum is generated by superposing Fourier modes with independent phases θ, uniformly distributed between $[0, 2\pi]$:

$$v_i(x_1, x_2) = \sum_{k_1, k_2} (k_1^2 + k_2^2)^{-2/3} \exp(\mathrm{i}[x_1 k_1 + x_2 k_2 + \theta]), \quad \theta \in [0, 2\pi]. \tag{34}$$

The two velocity components ($i = 1, 2$) are generated independently. Again, to obtain statistics comparable to those of the data, six 'images' are generated and are analysed in exactly the same fashion as the real data.

When using the top-hat or Gaussian filter, the (τ_{ij}, L_{ij}) correlation coefficients are not zero. We obtain values of about $\rho \sim 0.3$. The reason for this result is that a given Fourier mode that exists in the random-phase data can contribute to both the small- and large-scale box averages (or Gaussian averages). Thus some correlation between small and large scales exists. When a cut-off filter is employed, no such correlation is observed, by construction.

Very importantly, the (τ_{ij}, L_{ij}) correlation for the turbulence data is almost twice that

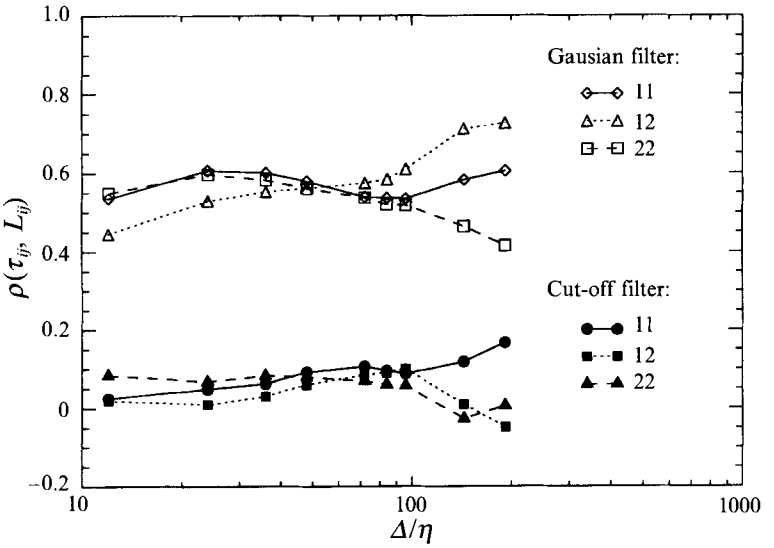

FIGURE 19. Correlation coefficients between τ_{ij} and L_{ij} as function of filter width for the Gaussian and for the cut-off filters.

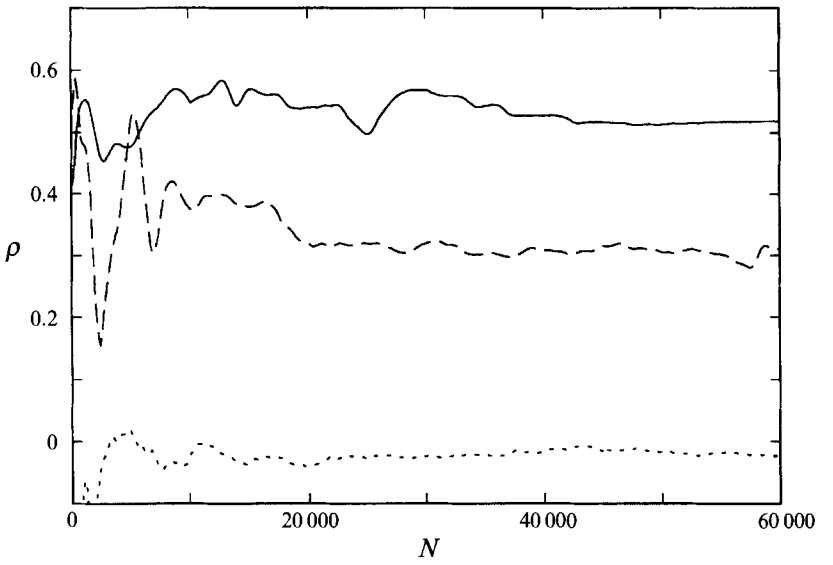

FIGURE 20. Running convergence plot for the correlations between L_{11} and τ_{11} as computed from the turbulence data (solid line), from the random-phase synthetic field, displaying a $-\frac{5}{3}$ spectrum (dashed line) and white noise (dotted line). A top-hat filter with $\Delta = 14\delta$ has been used.

of the random-phase data, outside any uncertainty due to statistical convergence (see figure 20). This difference is a direct result of the non-Gaussian nature of real turbulent flows. The degree of spatial intermittency of the SGS stresses is more pronounced for the real data than for the random-phase Fourier modes. In consequence, the correlation that exists across scales is more pronounced, because fewer but more intense events dominate the correlation. We would expect this trend to grow as the scale Δ becomes smaller, but the present data do not contain a large enough range of scales to allow quantification of this assertion.

Thus, the scale coherence manifested in the (τ_{ij}, L_{ij}) correlation has a 'kinematic' component (due to spectral characteristics) which is present even in random-phase data, and a 'dynamic' component (due to spatial intermittency) which a random-phase signal does not possess.

6.4. *Comparison at the vector level*

In this section we compare the divergence of the real and modelled stresses. The divergence is approximated as follows:

$$(\nabla\cdot\boldsymbol{\tau})_i \approx \frac{\partial\tau_{i1}}{\partial x_1}+\frac{\partial\tau_{i2}}{\partial x_2}, \quad i=1,2. \tag{35}$$

As required by measurement limitations, we cannot include the third term representing the effect of the velocity fluctuations normal to the image. We have computed the correlation coefficients between the elements of $\nabla\cdot\boldsymbol{\tau}$ and $\nabla\cdot\boldsymbol{L}$ using the above approximations. The results are typically close to $\rho\sim 0.4$, i.e. 30% lower than for the tensor elements themselves. A possible cause for the difference in correlation coefficients is the mismatch in characteristic lengthscales between the fields τ_{ij} and L_{ij}. The corresponding correlation coefficients for the divergence of the Smagorinsky model, however, are still much lower ($\rho<0.2$). A more systematic study of the SGS stress divergence is left as future task to be undertaken once more complete (three-dimensional) experimental data become available (see concluding remarks in §10).

7. Relation between stresses and the velocity gradient tensor: the nonlinear model

For the purpose of establishing a relationship between L_{ij} and nonlinear SGS models, let us approximate the velocity field $\tilde{u}_i$ as a piecewise-linear vector field in the neighbourhood of each point on the Δ-mesh. Similar arguments have been employed before to estimate the Leonard and cross-stresses (Leonard 1974; Clark *et al.* 1979; Horiuti 1993). Let us denote some given point of the Δ-mesh by $\boldsymbol{x}^0$. The procedure will be to evaluate L_{ij} by a top-hat filtering applied to the assumed linear velocity field around $\boldsymbol{x}^0$.

By expanding $\tilde{u}_i$ in Taylor series around $\boldsymbol{x}^0$ we can write

$$\tilde{u}_i(\boldsymbol{x}) = \tilde{u}_i(\boldsymbol{x}^0)+\tilde{A}_{ik}(\boldsymbol{x}^0)(x_k-x_k^0)+\ldots. \tag{36}$$

Nevertheless, we argue that this approximation is, in fact, not very good. The reason is that the linearized field, once filtered by the top-hat filter, produces a mean value equal to $\tilde{u}_i(\boldsymbol{x}^0)$, which is different from the real 'local average' $\bar{\tilde{u}}_i$:

$$\frac{1}{(2\Delta)^3}\int_{x_1^0-\Delta}^{x_1^0+\Delta}\int_{x_2^0-\Delta}^{x_2^0+\Delta}\int_{x_3^0-\Delta}^{x_3^0+\Delta}(\tilde{u}_i(\boldsymbol{x}^0)+\tilde{A}_{ik}(\boldsymbol{x}^0)(x_k-x_k^0))\,\mathrm{d}x_1\,\mathrm{d}x_2\,\mathrm{d}x_3 = \tilde{u}_i(\boldsymbol{x}^0)\neq\bar{\tilde{u}}_i. \tag{37}$$

This defect can easily be remedied by using, instead of $\tilde{u}_i(\boldsymbol{x}^0)$, the real average velocity as reference velocity, yielding

$$\tilde{u}_i(\boldsymbol{x}) \approx \bar{\tilde{u}}_i(\boldsymbol{x}^0)+\tilde{A}_{ik}(\boldsymbol{x}^0)(x_k-x_k^0). \tag{38}$$

With this more realistic approximation for $\tilde{u}_i(\boldsymbol{x})$ in the neighbourhood of $\boldsymbol{x}^0$, one can now evaluate the expression for L_{ij}. The result is the following:

$$L_{ij}(\boldsymbol{x}^0) \approx \tfrac{1}{3}\Delta^2\tilde{A}_{ik}(\boldsymbol{x}^0)\,\tilde{A}_{jk}(\boldsymbol{x}^0). \tag{39}$$

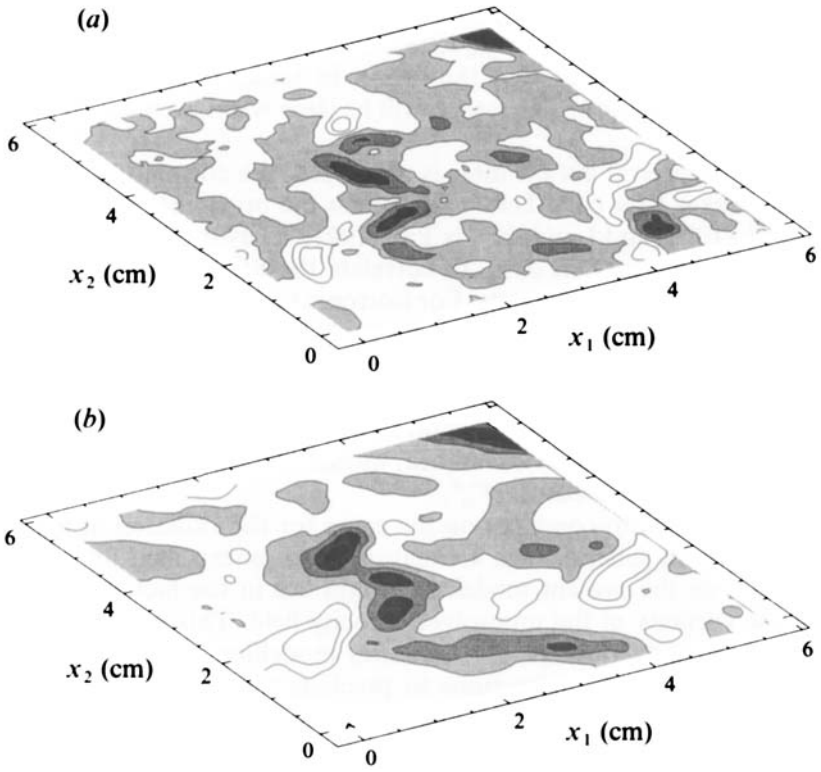

FIGURE 21. Comparison of (*a*) a contour plot of the real SGS stress element τ_{12} with (*b*) a contour plot of $\Delta^2 \tilde{A}_{1k} \tilde{A}_{2k}$. Contours in (*a*) start at $-0.0048\ \mathrm{m^2\ s^{-2}}$ (dark) and continue at intervals of $0.00096\ \mathrm{m^2\ s^{-2}}$. Contours in (*b*) start at $-0.008\ \mathrm{m^2\ s^{-2}}$ (dark) and continue at intervals of $0.0018\ \mathrm{m^2\ s^{-2}}$.

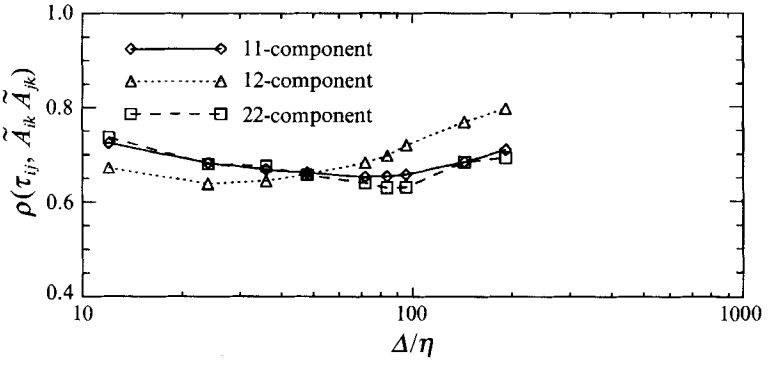

FIGURE 22. Correlation coefficients between τ_{ij} and $\tilde{A}_{ik}\tilde{A}_{jk}$ as function of filter width (using the top-hat filter). The different lines are for different tensor elements.

The combination of this result with our previous arguments linking τ_{ij} to L_{ij} yields the following nonlinear model for the SGS stress:

$$\mathscr{T}_{ij}^{(A)} = c_A \Delta^2 \tilde{A}_{ik} \tilde{A}_{jk}. \tag{40}$$

Figure 21 shows contour plots of τ_{12} and $\mathscr{T}_{12}^{(A)}$ (with $c_A = 1$), while figure 22 shows the correlation coefficients $\rho(\tau_{ij}, \mathscr{T}_{ij}^{(A)})$ for different values of Δ. We remark that the test

is a consistent one, because $\tilde{A}_{ij}$ has been evaluated from the data at the Δ-grid level. As can be seen, the correlation is comparable to that observed in the L_{ij} formulation. However, we shall argue later that the model in terms of L_{ij} is preferable to the velocity-gradient formulation. The reason will be clear when we consider the near-wall behaviour in §9.

Note that if the spectral cut-off filter is employed, the correlation between τ_{ij} and $\mathscr{T}_{ij}^{(A)}$ is much weaker ($\rho \sim 0.2$). This may explain the previously negative findings of Meneveau *et al.* (1992) and Lund & Novikov (1992). They tried, using cut-off filtering of low-Reynolds-number DNS data, to correlate the SGS stresses with a variety of combinations of the velocity gradients. For isotropic turbulence, no strong correlations were found, which is also consistent with the low correlation for the similarity model L_{ij} using the cut-off filter. However, for shear flows there was considerable indication of nonlinear dependencies between τ_{ij} and the resolved velocity gradients, even when using the cut-off filter. These trends remain to be explained. In addition, we point out that Horiuti (1993) has proposed a nonlinear model which contains, as one of its many terms, an expression equivalent to $\mathscr{T}_{ij}^{(A)}$.

Finally, it is pertinent to comment on the cause for the violation of material-frame indifference in (40). In general, such a violation is not unexpected for turbulent flows (Lumley 1970). For the present model, its origin lies in the fact that the real stress depends on the vorticity of the unresolved velocity field. This vorticity is then linked to the resolved vorticity through the similarity modelling. One expects the spectral closeness of the turbulence interactions to preclude the separation of scales that is required for the appearance of frame-invariant constitutive relations. This feature is explicitly taken into account in the similarity model.

8. Energy dissipation and backscatter control

Figure 23 shows contour maps of the real and modelled local SGS energy flux. These are computed according to

$$\Pi_\tau = -\tau_{ij}\tilde{S}_{ij} \quad \text{and} \quad \Pi_L = -L_{ij}\tilde{S}_{ij}. \tag{41}$$

The tensor contractions have been approximated in terms of the measured elements in the same fashion as (23). The fact that both fields exhibit some coarse resemblance is due to the considerable correlation that exists between τ_{ij} and L_{ij}. Significant portions of the flow where backscatter exists ($\Pi < 0$) appear in both the 'real' and 'modelled' fields of energy flux. From these results it may appear that the modelling based on L_{ij} can capture backscatter in a reasonable manner. However, as outlined in § 1, experience from LES calculations with similarity models (see e.g. Bardina *et al.* 1980) shows that calculations become unstable because such models are not dissipative enough. The remedy has been to add a term of the eddy-viscosity type, yielding 'mixed models' (Bardina *et al.* 1980; Horiuti 1993, etc.). We have tested the following version of the mixed model:

$$\mathscr{T}_{ij}^{mix} = -2(c_s\Delta)^2|\tilde{S}|\tilde{S}_{ij} + c_L L_{ij}. \tag{42}$$

We have chosen the Smagorinsky coefficient in the usually employed range $c_s = 0.1$ to 0.2. Since we found the level of fluctuations of L_{ij} to be of the same order of magnitude as those of τ_{ij}, we set $c_L = 1$. Interestingly, the correlation coefficients between τ_{ij} and $\mathscr{T}_{ij}^{mix}$ that are measured from our data sets are essentially the same as those of the stress-similarity model alone. The main reason is that the typical magnitudes of the Smagorinsky term are much smaller than those of L_{ij}, and thus do not affect its correlation with the real stress (for a more detailed discussion, see Liu, Meneveau &

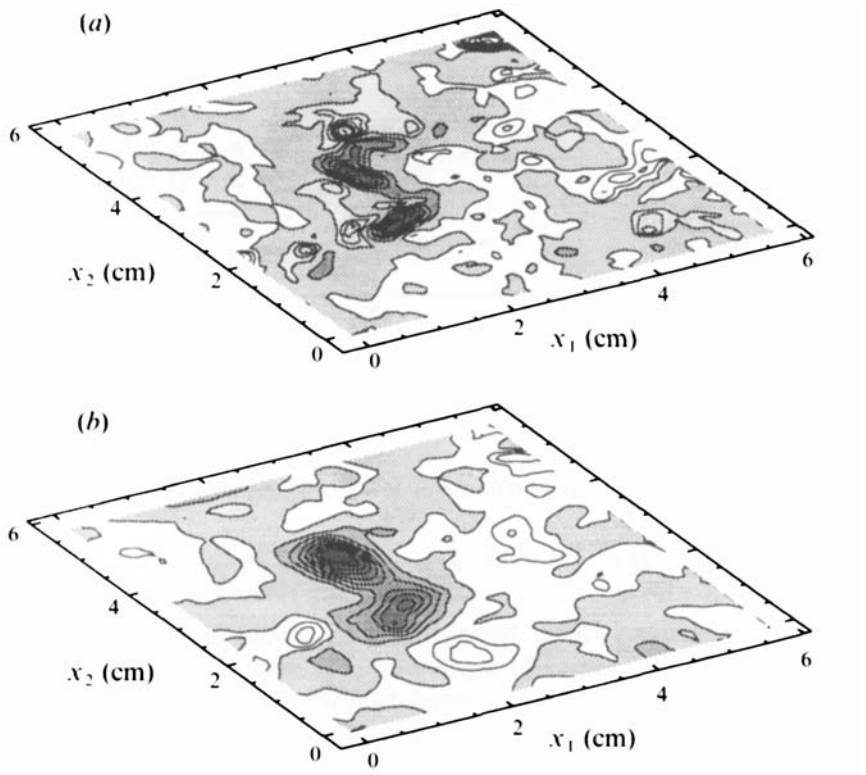

FIGURE 23. Contour plots of SGS energy flux. (*a*) The flux estimated from the real SGS stress, $\Pi_\tau = -\tau_{ij}\tilde{S}_{ij}$. (*b*) The SGS flux implied by the modelled stress $\Pi_L = -L_{ij}\tilde{S}_{ij}$. Darkest grey corresponds to a maximum value of 0.0288 $m^2\,s^{-3}$, and the contours are spaced by constant increments of $-0.0036\ m^2\,s^{-3}$. White regions denote negative values.

Katz 1994*a*). However, since the Smagorinsky term is well correlated with the resolved strain rate, it systematically contributes to positive dissipation of energy. From this point of view, such a mixed model appears to be a very desirable option (see Zang, Street & Koseff 1993 and Akhavan, Ansari & Mangiavacci 1993 for recent numerical work using mixed models).

In §9 we shall discuss some difficulties that occur near solid walls when adding eddy-viscosity terms. Therefore, it is useful to suggest a possible alternative which consists in selectively weighting the similarity stress with the amount of energy dissipation that it is generating. The SGS dissipation depends on the alignment between the two tensors L_{ij} and $\tilde{S}_{ij}$, which can be quantified by the following dimensionless invariant:

$$I_{LS} = -\frac{L_{pq}\tilde{S}_{pq}}{(L_{mr}L_{mr})^{1/2}(\tilde{S}_{kn}\tilde{S}_{kn})^{1/2}}. \tag{43}$$

One can show that I_{LS} is bounded between -1 and 1. We now postulate a similarity model in which there is some dependence on the strain-rate tensor, through the following formulation:

$$\mathscr{T}_{ij}^{(fL)} = c_L f(I_{LS})\, L_{ij}. \tag{44}$$

Here $f(I_{LS})$ is a dimensionless scalar function which depends on I_{LS}. If we choose

$$f_1(I_{LS}) = I_{LS}, \tag{45}$$

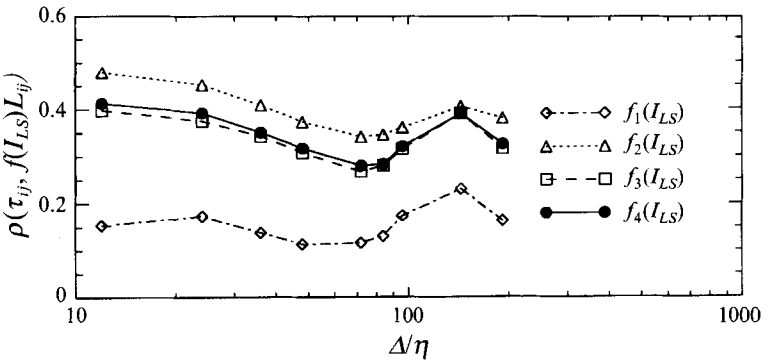

FIGURE 24. Correlation between τ_{ij} and $f(I_{LS})\,L_{ij}$, for different choices of the backscatter control functions $f(I)$ averaged over the 11-, 12- and 22-components.

we change the sign of the stress whenever it would generate backscatter and

$$\Pi = -\mathscr{T}^{(fL)}\tilde{S}_{ij} = \frac{c_L(L_{pq}\tilde{S}_{pq})^2}{(L_{mr}L_{mr})^{1/2}(\tilde{S}_{kn}\tilde{S}_{kn})^{1/2}}$$

is evidently positive everywhere. Nevertheless, we would obtain a positive correlation between τ_{ij} and $\mathscr{T}^{(fL)}$ whenever L_{ij} is preferentially counter-aligned with the strain rate ($I_{LS} > 0$) while obtaining a negative correlation when $I_{LS} < 0$. The overall correlation is thus very low. On the other hand, if we define

$$f_2(I_{LS}) = \begin{cases} I_{LS} & \text{if} \quad I_{LS} \geqslant 0 \\ 0 & \text{if} \quad I_{LS} < 0 \end{cases} \tag{46}$$

we 'turn off' the stress in the backscattering regions, thus avoiding the cancellation of the positive correlation that exists in the dissipative regions. Another choice could be

$$f_3(I_{LS}) = \begin{cases} 1 & \text{if} \quad I_{LS} \geqslant 0 \\ 0 & \text{if} \quad I_{LS} < 0, \end{cases} \tag{47}$$

which weights all dissipative regions uniformly, thereby increasing the correlation as compared to the choice of (46). The discontinuity at $I_{LS} = 0$ could, however, generate numerical difficulties. A possibility which is smooth at the origin but close to uniform over much of the interval $0 < I_{LS} < 1$ is given by the empirical choice

$$f_4(I_{LS}) = \begin{cases} [1 - \exp(-\gamma I_{LS}^2)] & \text{if} \quad I_{LS} \geqslant 0 \\ 0 & \text{if} \quad I_{LS} < 0. \end{cases} \tag{48}$$

A mild sloping behaviour can be obtained by the (arbitrary) choice $\gamma = 10$. In figure 24, the measured correlation coefficients that result from each choice for the function $f(I_{LS})$ are plotted as a function of Δ. As can be seen, the correlation is considerably lower than the original value without backscatter control, or with the mixed model. Nevertheless, if for numerical reasons it is determined that backscatter control is needed, the choice of (48) enables us to maintain and exploit the stress similarity at least over the dissipative regions. Further work is needed to better model the backscatter without the risk of generating numerical instabilities.

Lund (1993) has recently found indications that the main cause for backscatter-related instability in numerical simulations is a mismatch of timescales between the real

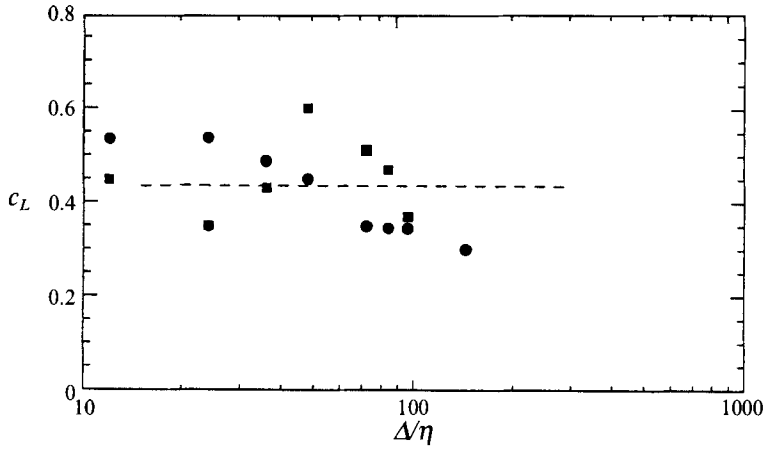

FIGURE 25. Circles: model constant c_L derived from the balance of SGS energy dissipation for the dissipative similarity model, as function of Δ (top-hat filter). Squares: model constant c_L^{dyn} derived from the dynamic model, based solely on the resolved velocity field.

backscattering events and the modelled ones based on the resolved field. Our experimental data consist of instantaneous single-time fields and so, for now, we cannot address this issue. The problem pointed out by Lund (1993), however, is also likely to occur with the present similarity model if no backscatter control is performed: the fluctuations of L_{ij} are expected to occur at a slower pace than those of the real stresses, and so the modelled backscatter events will last longer than the real ones.

We close this section with some remarks about the model coefficient c_L appearing in (44). It can be estimated (Meneveau 1994) from the data by requiring that the correct amount of energy dissipation be taking place,

$$-\langle \tau_{ij} \tilde{S}_{ij} \rangle = -c_L \langle f(I_{LS}) L_{ij} \tilde{S}_{ij} \rangle. \tag{49}$$

The required tensor contractions are computed using the same approximations as before. The calculated coefficient c_L is plotted as a function of Δ in figure 25 (solid circles). A top-hat filter has been employed. The statistical quantities that are being evaluated to calculate c_L are third-order moments and we observe some difficulties with statistical convergence. Thus we do not ascribe much significance to the variability seen in figure 25. The results suggest a value of $c_L = 0.45 \pm 0.15$.

9. Near-wall behaviour and dynamic modelling

One of the main advantages of similarity models is their behaviour across different flow regimes. If the flow is non-turbulent but, for example, highly strained, the eddy-viscosity closures will generate too much energy dissipation, while a model based on resolved stresses such as L_{ij} will give low (or zero) values, as required. The dynamic procedure applied to the Smagorinsky model (Germano *et al.* 1991) has a similar property because the eddy viscosity is weighted by L_{ij}. Another important change in regime occurs near solid boundaries, which we shall briefly consider below. The discussion to follow is only relevant under the assumption that the LES has many grid points near the wall and is able to resolve the viscous sublayer. Let the x_2 direction be the normal to the surface and let us consider the flow at some instant of time, very

near the wall. We perform a Taylor series expansion at the wall of the instantaneous velocity field in the x_2 direction. We find $u_1 \sim x_2$, $u_2 \sim x_2^2$ and $u_3 \sim x_2$. The near-wall scaling of the real instantaneous SGS stress tensor is therefore as follows:

$$\tau_{11} \sim x_2^2, \quad \tau_{22} \sim x_2^4, \quad \tau_{33} \sim x_2^2, \quad \tau_{12} \sim x_2^3, \quad \tau_{13} \sim x_2^2, \quad \tau_{23} \sim x_2^3.$$

If one defines the stress by subtracting its isotropic part, the result is identical except for τ_{22} which now would scale like the other two normal stresses, $\tau_{22} \sim x_2^2$. For the Smagorinsky model with no wall functions or dynamic model, the scaling with respect to x_2 is quite different than that of the real stresses. It is as follows:

$$\mathscr{T}_{11}^{(S)} \sim x_2, \quad \mathscr{T}_{22}^{(S)} \sim x_2, \quad \mathscr{T}_{33}^{(S)} \sim x_2, \quad \mathscr{T}_{12}^{(S)} \sim \text{const.}, \quad \mathscr{T}_{13}^{(S)} \sim x_2, \quad \mathscr{T}_{23}^{(S)} \sim \text{const.}$$

A very desirable feature of the dynamic model

$$\tau_{ij} = \frac{L_{mn} M_{mn}}{M_{pq} M_{pq}} |\tilde{S}| \tilde{S}_{ij}, \quad M_{pq} = 4|\bar{\tilde{S}}| \bar{\tilde{S}}_{pq} - \overline{|\tilde{S}| \tilde{S}_{pq}} \tag{50}$$

is that it can correct the behaviour of the most relevant term, τ_{12} (Germano *et al.* 1991; Piomelli 1993). Using the fact that the scaling of each element of L_{ij} and M_{ij} is the same as that of τ_{ij} and $\tilde{S}_{ij}$, respectively, one obtains the near-wall scalings $L_{mn} M_{mn} \sim x_2^3$ and $M_{pq} M_{pq} \sim$ const. It follows that the dynamic Smagorinsky model scales (instantaneously) as

$$\mathscr{T}_{11}^{(S)} \sim x_2^4, \quad \mathscr{T}_{22}^{(S)} \sim x_2^4, \quad \mathscr{T}_{33}^{(S)} \sim x_2^4, \quad \mathscr{T}_{12}^{(S)} \sim x_2^3, \quad \mathscr{T}_{13}^{(S)} \sim x_2^4, \quad \mathscr{T}_{23}^{(S)} \sim x_2^3$$

near the wall. Therefore, only the τ_{12} and τ_{23} elements display the right behaviour. If the wall is a plane and the mean flow direction is x_1, then on average τ_{12} is the only non-zero element. Its average value is needed for the calculation of the skin friction. However, if one is interested in predicting, for instance, the spectrum of wall-pressure fluctuations, it is easy to show that the subgrid-scale contributions arise from second-order moments of the SGS stress. Therefore, correct instantaneous scaling of the other tensor elements should also be desirable. For dynamic control purposes, realistic descriptions of individual realizations is also of importance.

Next we consider the proposed stress-similarity model, without backscatter control. It is obvious that each term displays the correct near-wall behaviour. However, as soon as we multiply L_{ij} by a backscatter control function $f(I_{LS})$, this property is upset: the scaling of $L_{pq} \tilde{S}_{pq}$ is $L_{pq} \tilde{S}_{pq} \sim x_2^3$ and that of $L_{pq} L_{pq}$ is $\sim x_2^4$. Thus $I_{LS} \sim x_2$ as one approaches the wall. Suppose that $f(I_{LS}) \sim I_{LS}^{\alpha}$ near the origin (in the case of (48) we have $\alpha = 2$). Then the near-wall behaviour of the model is

$$\left.\begin{array}{lll} \mathscr{T}_{11}^{(fL)} \sim x_2^{2+\alpha}, & \mathscr{T}_{22}^{(fL)} \sim x_2^{4+\alpha}, & \mathscr{T}_{33}^{(fL)} \sim x_2^{2+\alpha}, \\ \mathscr{T}_{12}^{(fL)} \sim x_2^{3+\alpha}, & \mathscr{T}_{13}^{(fL)} \sim x_2^{2+\alpha}, & \mathscr{T}_{23}^{(fL)} \sim x_2^{3+\alpha}, \end{array}\right\} \tag{51}$$

which is clearly unsatisfactory. This erroneous near-wall behaviour can be fixed, as shown in the next section.

9.1. *A dynamic stress-similarity model*

In order to evaluate the coefficient c_L which appears in the similar-stress model and also to attempt to eliminate the previously found problem near solid walls, we apply the dynamic procedure to the present model. For this purpose we define a stress analogous to L_{ij} but at twice the scale

$$Q_{ij} = \widehat{\bar{\tilde{u}}_i \bar{\tilde{u}}} - \bar{\hat{\tilde{u}}}_i \bar{\hat{\tilde{u}}}_j, \tag{52}$$

where, as before, the *hat* represents filtering at a scale 4Δ and the *overbar* represents filtering at scale 2Δ. We recall that these operations only use data available on the Δ-grid. Defining

$$M_{ij} = f(I_{SQ})\, Q_{ij} - \overline{f(I_{LS})\, L_{ij}}, \tag{53}$$

where

$$I_{QS} = \frac{Q_{mn}\,\tilde{\bar{S}}_{mn}}{|Q|\,|\tilde{\bar{S}}|},$$

the dynamic similar-stress model (Germano *et al.* 1991; Lilly 1992) can be written as

$$\mathscr{T}_{ij}^{(lo)} = \left(\frac{L_{mn}\,M_{mn}}{M_{pq}\,M_{pq}}\right) f(I_{LS})\, L_{ij}. \tag{54}$$

If there is alignment between strain rate and stresses (backscatter) both at the grid level and at the test-filter level, then M_{ij} can be identically zero due to the control function $f(I)$. In such circumstances one could set the entire expression to zero. How much local smoothing needs to be performed to avoid problems due to locally very small values of $|M|$ needs to be decided based on testing in LES. One could perform some averaging, in which case the model will read

$$\mathscr{T}_{ij}^{(av)} = \frac{\langle L_{mn}\,M_{mn}\rangle}{\langle M_{pq}\,M_{pq}\rangle} f(I_{LS})\, L_{ij}. \tag{55}$$

A formulation based on an integral equation for the model constant (Ghosal, Lund & Moin 1992) is another option.

Returning to the question of near-wall behaviour, we find that the scaling of the elements of M_{ij} is the same as that of the terms appearing in (51). Therefore, $L_{mn}\,M_{mn} \sim x_2^{4+\alpha}$ and $M_{mn}\,M_{mn} \sim x_2^{4+2\alpha}$. It follows that the model coefficient diverges as $x_2^{-\alpha}$, cancelling the x_2^{α} scaling of the function $f(I_{LS})$. The correct scaling embodied by L_{ij} is thus restored. In conclusion, the model of (54) or (55) appears to possess many desirable qualities.

It is interesting to notice that the nonlinear model in terms of the resolved velocity-gradient tensor has incorrect near-wall scaling, which is not corrected even when a dynamic procedure is employed. The reason for this deficiency is that the Taylor-series expansion used to relate L_{ij} to the velocity gradients does not explicitly take into account the presence of the wall.

9.2. *Dynamic model constant obtained from the experimental data*

The evaluation of the model coefficient c_L in §8 required knowledge of the real stress τ_{ij}, which is not available in an actual LES. The dynamic model allows the evaluation of the model constant from the resolved field, a procedure that can also be applied to the experimental data. If we suppose that the averaging in (55) is an ensemble and spatial average over a domain of size comparable to our data set, we can evaluate the dynamic model constant as follows:

$$c_L^{dyn} = \langle L_{mn}\,M_{mn}\rangle / \langle M_{pq}\,M_{pq}\rangle. \tag{56}$$

The squares in figure 25 display the value of c_L^{dyn} evaluated from the experimental data, as a function of Δ (using top-hat filter). The averaging is performed over the six images. A value of about $c_L^{dyn} \sim 0.45 \pm 0.15$ can again be deduced. It is encouraging to find a value which is of the same order of magnitude as that obtained before from the energy dissipation balance (circles). The spread of the results is quite large, however, and is probably due to the limited size of our data sample.

10. Summary and conclusions

Particle displacement velocimetry has been employed to measure a set of instantaneous velocity vector maps in the far field of a turbulent round jet. The energy spectrum of the data was shown to match the Kolmogorov spectrum quite well, with over a decade of inertial range. By suitably filtering the data at inertial-range scales $\Delta(\eta \ll \Delta < l)$, *a priori* analysis of several models for the turbulence subgrid stresses was performed. Since only two out of three velocity components were measured, some assumptions had to be made when evaluating tensor contractions. Also, since the data were obtained in a planar section of the flow, the filtering was done in two rather than three dimensions. These are the limitations of the present approach as compared to the analysis of DNS data. However, we were able to study a flow with realistic boundary conditions at a much higher Reynolds number ($R_\lambda \sim 310$).

As a first step, the SGS stress field was measured and its properties were documented. Next, the correlation coefficients with the strain rate (as in the Smagorinsky model) were shown to be very small ($\rho \sim 0.15$), implying that locally the eddy-viscosity closures perform very poorly. While this finding is in agreement with numerous previous results from *a priori* analysis of DNS data, we have now been able to confirm them in a much higher Reynolds-number flow. Next, the measured SGS flux of kinetic energy was shown to be of the same order of magnitude as the overall energy dissipation $u'^3/l \sim \epsilon$. By examining spatial features of the flux of energy at a larger scale and how it is divided into 'local' and 'not-so-local' contributions, it became apparent that the flow fields in consecutive scales of motion must have some similarity.

For the rest of the paper the focus was on documenting this similarity in various ways, and on exploiting it in formulating a new similarity model. Some similarity was observed between the velocity fields in consecutive bands representing the motion of different scales. Care was taken not to use overlapping information that could artificially increase this similarity. A natural choice for a model was shown to be a self-similar rescaling of the expression relating the stress to the velocity fields in two bands surrounding the cut-off scale. This procedure was shown to lead to a model which represents the SGS stress $\widetilde{u_i u_j} - \tilde{u}_i \tilde{u}_j$ by the stress computed from the resolved field, $L_{ij} = \widetilde{\tilde{u}_i \tilde{u}_j} - \bar{\tilde{u}}_i \bar{\tilde{u}}_j$. The experimental data were used to show that the correlation coefficient for this model was much higher ($\rho \sim 0.6$) than that of eddy-viscosity closures.

The influence of filter type was studied and it was found that the correlation between stresses (real and modelled) is very small if a cut-off filter is employed. It was argued that the spatially non-local nature of this filtering is responsible for destroying subtle relationships that exist between local flow structures. A brief comparison with the model of Bardina *et al.* (1980) was made, and advantages of the present approach were pointed out. Also, it was shown that the measured correlation for the new similarity model significantly exceeded the correlation coefficient for the same quantities evaluated from a Gaussian random field (with a $-\frac{5}{3}$ spectrum). This dynamical effect was attributed to the spatial intermittency of turbulence, which tends to concentrate the fluctuations in subsets of the available space, i.e. in compact 'structures' for which the scale coherence is more pronounced than for the Gaussian fields. It was checked that no correlation exists if the same procedure is applied to white noise. A connection to nonlinear models was then made, by local linearization of the resolved velocity field, and an evaluation of L_{ij}. The result involved the entire velocity-gradient tensor and correlations between the model and real stress elements that were comparable to the proposed similarity model were found. Since previous similarity SGS models have

exhibited practical difficulties, possibly due to errors that are incurred in the prediction of backscatter, a particular version of the mixed model was studied. It was found that the addition of an eddy-viscosity (Smagorinsky) expression had little effect on the correlation, because of the low magnitude of the eddy-viscosity term relative to the similarity term.

As an alternative to the mixed model, a modification to the stress-similarity model was proposed. It involves the use of an empirical weighting function $f(I_{LS})$ which depends on the alignment between stress and strain rate. Several options for the function $f(I_{LS})$ were outlined, all of which had, however, the effect of diminishing the overall correlation between the real and modelled stress, to varying degrees. Since the model contained an undetermined numerical coefficient c_L, it turned out to be a good candidate to be subjected to the dynamic procedure of Germano *et al.* (1991). It was shown that this procedure allowed a dynamical determination of the coefficient. This dynamic model (as opposed to the dynamic Smagorinsky or mixed models) displayed proper near-wall behaviour for all tensor elements, if implemented in an LES with fully resolved viscous sublayer.

In conclusion, experimental data at high Reynolds number has been employed to formulate a stress-similarity model which displays markedly larger correlation with the real stress than eddy-viscosity closures do. Having established these features from the real physics as manifested in the experimental data, it remains to be seen how the model behaves in numerical simulations.

Many open questions serve as motivation for future work in this area. It would be desirable to find possible relations between the difference $\mathscr{T}_{ij}-\tau_{ij}$ (the 'unexplained data') and the resolved flow variables. Such a study may lead to further increases in the correlation coefficients. For this purpose we plan to perform conditional averaging, for which more data sets need to be considered to guarantee statistical convergence (Liu, Meneveau & Katz 1994*b*). Projection pursuit regression (see Meneveau *et al.* 1992) may also be helpful for this purpose. More complete data sets, including the third component of the velocity and three-dimensional filtering can be obtained using new measurement techniques such as HPDV (holographic particle displacement velocimetry). It would be of considerable interest to verify the present results with more complete data, for which no assumptions (such as isotropy or two-dimensional filtering) would have to be made. Another feature which we would like to study in detail using three-dimensional velocity measurements is the stress divergence $\nabla\cdot\boldsymbol{\tau}$. Finally, questions associated with local averaging when using the dynamic model could also be directly addressed from experimental data.

C.M. wishes to acknowledge fruitful discussions with O. Knio and M. Karweit. The authors are grateful for the financial support from the Fluid Dynamics Division of the Office of Naval Research (Code 332FD, grant N00014-92-J-1109, monitored by Dr P. Purtell).

Appendix A. Radial Kolmogorov spectrum in two dimensions

In isotropic turbulence, the two-dimensional spectrum obtained by Fourier transforming a two-dimensional section of the velocity field at constant x_3, can be written as

$$\phi_{ij}(k_1,k_2) = 2\int_0^\infty \frac{E(k)}{4\pi k^2}\left(\delta_{ij}-\frac{k_i k_j}{k^2}\right)\mathrm{d}k_3, \tag{A 1}$$

where $k^2 = k_1^2 + k_2^2 + k_3^2$. If we consider $i = j = 1$ and integrate over an annulus of constant $\kappa = (k_1^2 + k_2^2)^{1/2}$, we obtain

$$\phi_{11}(\kappa) = \frac{1}{2\pi}\int_0^\infty \int_0^{2\pi} \frac{E(k)}{k^2}\left(1 - \frac{\kappa^2}{k^2}\cos^2\theta\right)\kappa \, \mathrm{d}\theta \, \mathrm{d}k_3$$

$$= \int_0^\infty \kappa \frac{E((\kappa^2 + k_3^2)^{1/2})}{\kappa^2 + k_3^2}\left(1 - \frac{1}{2}\frac{\kappa^2}{\kappa^2 + k_3^2}\right)\mathrm{d}k_3. \tag{A 2}$$

Replacing the power-law form $E(k) = ck^{-\alpha}$ and evaluating the integrals leads to

$$\phi_{11}(\kappa) = c\kappa^{-\alpha}\left\{\frac{\Gamma(\frac{1}{2})\,\Gamma(\frac{1}{2}(\alpha+1))}{2\Gamma(\frac{1}{2}\alpha+1)} - \frac{\Gamma(\frac{1}{2})\,\Gamma(\frac{1}{2}(\alpha+1))}{4\Gamma(\frac{1}{2}\alpha+2)}\right\}$$

$$\approx 0.535378 c\kappa^{-5/3} \quad \text{for} \quad \alpha = \tfrac{5}{3}. \tag{A 3}$$

Therefore, the correction prefactor needed to transform the three-dimensional power law to the radial two-dimensional form is $\beta \approx 0.535$.

REFERENCES

AKHAVAN, R., ANSARI, A. & MANGIAVACCI, N. 1993 Subgrid-scale modeling of energy transfer in turbulent shear flows. *Bull. Am. Phys. Soc.* **38**, 2231.

AKSELVOLL, K. & MOIN, P. 1993 Application of the dynamic localization model to large-eddy simulation of turbulent flow over a backward facing step. In *Engineering Applications of Large Eddy Simulations* (ed. U. Piomelli & S. Ragab) ASME-FED, vol. 162, p. 1.

BARDINA, J., FERZIGER, J. H. & REYNOLDS, W. C. 1980 Improved subgrid scale models for large eddy simulation. *AIAA Paper* 80-1357.

CHASNOV, J. R. 1991 Simulation of the Kolmogorov inertial subrange using an improved subgrid model. *Phys. Fluids* A **3**, 188.

CHOLLET, J. & LESIEUR, M. 1981 The parameterization of small scales of three-dimensional isotropic turbulence utilizing spectral closures. *J. Atmos. Sci.* **38**, 2747.

CLARK, R. A., FERZIGER, J. H. & REYNOLDS, W. C. 1979 Evaluation of subgrid models using an accurately simulated turbulent flow. *J. Fluid Mech.* **91**, 1.

DEARDORFF, J. W. 1970 A numerical study of three-dimensional turbulent channel flow at large reynolds numbers. *J. Fluid Mech.* **41**, 453.

DONG, R., CHU, S. & KATZ, J. 1992 Quantitative visualization of the flow structure within the volute of a centrifugal pump, part a: Technique. *Trans. ASME* I: *J. Fluids Engng* **114**, 390.

FERZIGER, J. H. 1977 Large eddy numerical simulations of turbulent flows. *AIAA J.* **15**, 1261.

GANAPATHY, S. & KATZ, J. 1993 Lift and drag forces on bubbles entrained by a vortex ring within non-uniform unsteady flows. In '*Cavitation and Multiphase Flow Forum*', *Washington DC, June, 1993*, p. 165. ASME.

GERMANO, M. 1986 A proposal for a redefinition of the turbulent stresses in the filtered Navier–Stokes equations. *Phys. Fluids* **29**, 2323.

GERMANO, M. 1992 Turbulence: the filtering approach. *J. Fluid Mech.* **238**, 325.

GERMANO, M., PIOMELLI, U., MOIN, P. & CABOT, W. H. 1991 A dynamic subgrid-scale eddy viscosity model. *Phys. Fluids* A **3**, 1760.

GHOSAL, S., LUND, T. S. & MOIN, P. 1992 A local dynamic model for large eddy simulation. In *Center for Turbulence Research, Annual Research Briefs, Stanford University*, vol. 3.

HORIUTI, K. 1989 The role of the Bardina model in large eddy simulation of turbulent channel flow. *Phys. Fluids* A **1**, 426.

HORIUTI, K. 1993 A proper velocity scale for modeling subgrid-scale eddy viscosities in large eddy simulation. *Phys. Fluids* A **5**, 146.

KRAICHNAN, R. H. 1976 Eddy viscosity in two and three dimensions. *J. Atmos. Sci.* **33**, 1521.

LEONARD, A. 1974 Energy cascade in large-eddy simulations of turbulent fluid flows. *Adv. Geophys.* **18**, 237.

LESLIE, D. C. & QUARINI, G. L. 1979 The application of turbulence theory to the formulation of subgrid modelling procedures. *J. Fluid Mech.* **91**, 65.

LILLY, D. K. 1967 The representation of small-scale turbulence in numerical simulation experiments. In *Proc. IBM Scientific Computing Symp. on Environmental Sciences*, p. 195.

LILLY, D. K. 1992 A proposed modification of the germano subgrid scale closure method. *Phys. Fluids* A **4**, 633.

LIU, S., MENEVEAU, C. & KATZ, J. 1994*a* Experimental study of similarity subgrid-scale models of turbulence in the far field of a jet. In *Direct and Large Eddy Simulation I* (ed. P. R. Voke, L. Kleiser and J. P. Chollet), pp. 37–48. Kluwer.

LIU, S., MENEVEAU, C. & KATZ, J. 1994*b* Experimental studies of similarity subgrid-scale models of turbulence using conditional averaging. ASME-FED (to appear).

LUMLEY, J. L. 1970 Towards a turbulent constitutive relation. *J. Fluid Mech.* **41**, 413.

LUND, T. 1993 Numerical experiments with highly-variable eddy viscosity models. In *Engineering Applications of Large Eddy Simulations* (ed. U. Piomelli & S. Ragab). ASME-FED, vol. 162, p. 7.

LUND, T. & NOVIKOV, E. A. 1992 Parametrization of subgrid-scale stress by the velocity gradient tensor. In *Center for Turbulence Research, Annual Research Briefs, Stanford University*, vol. 27.

MCMILLAN, O. J. & FERZIGER, J. H. 1979 Direct testing of subgrid-scale models. *AIAA J.* **17**, 1340.

MENEVEAU, C. 1994 Statistics of turbulence subgrid-scale stresses: Necessary conditions and experimental tests. *Phys. Fluids* **6**, 815.

MENEVEAU, C., LUND, T. & MOIN, P. 1992 Search for subgrid scale parametrization by projection pursuit regression. In *Proc. Summer Program 1992 Stanford University*, vol. IV, p. 61.

MÉTAIS, O. & LESIEUR, M. 1992 Spectral large-eddy simulation of isotropic and stably stratified turbulence. *J. Fluid Mech.* **239**, 157.

PIOMELLI, U. 1993 High Reynolds number calculations using the dynamic subgrid-scale stress model. *Phys. Fluids* A **5**, 1484.

PIOMELLI, U., MOIN, P. & FERZIGER, J. H. 1988 Model consistency in large eddy simulation of turbulent channel flows. *Phys. Fluids* **31**, 1884.

REYNOLDS, W. C. 1990 The potential and limitations of direct and large eddy simulations. In *Whither Turbulence? or Turbulence at Crossroads* (ed. J. L. Lumley), p. 313. Springer.

ROGALLO, R. & MOIN, P. 1984 Numerical simulation of turbulent flows. *Ann. Rev. Fluid. Mech.* **16**, 99.

SCHMIDT, H. & SCHUMANN, U. 1989 Coherent structure of the convective boundary layer derived from large-eddy simulations. *J. Fluid Mech.* **200**, 511.

SCHUMANN, U. 1975 Subgrid scale model for finite difference simulations of turbulent flows in plane channels and annuli. *J. Comput. Phys.* **18**, 376.

SMAGORINSKY, J. 1963 General circulation experiments with the primitive equations, i. the basic experiment. *Mon. Weath. Rev.* **91**, 99.

TENNEKES, H. & LUMLEY, J. L. 1972 *A First Course in Turbulence.* MIT Press.

YOSHIZAWA, A. 1989 Subgrid-scale modeling with a variable length scale. *Phys. Fluids* A **1**, 1293.

ZANG, Y., STREET, R. L. & KOSEFF, J. 1993 A dynamic mixed subgrid-scale model and its application to turbulent recirculating flows. *Phys. Fluids* A **5**, 3186.